# Mechanical Self-Organization of Particle Networks during Uniaxial Compression Yielding

Michio Tateno,[1] Yinqiao Wang,[1] and Hajime Tanaka[1,2,*]

[1]*Research Center for Advanced Science and Technology, The University of Tokyo, 4-6-1 Komaba, Meguro-ku, Tokyo 153-8904, Japan*

[2]*Department of Fundamental Engineering, Institute of Industrial Science, The University of Tokyo, 4-6-1 Komaba, Meguro-ku, Tokyo 153-8505, Japan*

(Received 8 July 2023; revised 7 November 2023; accepted 31 January 2024; published 4 March 2024)

Colloidal gels, sparse particle networks with large voids, are fundamental model systems of disordered porous materials. Unlike dense amorphous solids, they exhibit significant volumetric deformation while expelling solvents when subjected to external compression. Despite their importance in both natural and industrial settings, the relationship between their network microstructure and compressive yielding behavior has remained elusive. To address this problem, we employ confocal microscopy and a specially designed sample cell to observe the gravity-induced collapsing of colloidal gels at a single-particle level. The experimental insight gained is complemented by simulation results for gravitational collapse and homogeneous uniaxial compression. We find that, during compression, the microstructure of gels is uniquely determined solely by the local volume fraction. This relationship remains independent of the deformation strain history but is subtly influenced by the preparation history of the initial state. In contrast, compressive stress evolves as a unique function of local volume fraction, unaffected by both preparation and strain history, as long as the interparticle interaction remains identical. Moreover, we unveil that local yielding occurs in highly strained, narrow network domains, while highly stressed particles form chainlike structures to support the external stress. These findings suggest that colloidal gels undergoing compressive plastic deformation mechanically self-organize into a unique history-independent state to satisfy mechanical balance in a quasistatic condition, providing crucial microscopic insights into the compressive yielding behavior of particle network materials.

DOI: 10.1103/PhysRevX.14.011035

Subject Areas: Chemical Physics, Materials Science, Soft Matter

## I. INTRODUCTION

Colloidal gels, formed through physical (thermoreversible) attraction, are ideal model systems to study the structural and mechanical properties of fragile particle networks [1,2]. These networks exhibit unique, complex yielding behavior when subjected to external stress [3]. Studies on the evolution of microstructure under cyclic shear [4–7] and large shear strain [8–11] have revealed the importance of the pore-size scale topology and particle motions on the surface of the network, which is distinct from dense amorphous solids like glasses and dry granular materials [12]. The difference becomes even more pronounced in compressive deformation: unlike glassy systems, gels have the ability to considerably reduce their volume, effectively filling their large pores while expelling solvents.

Compressive yielding of particle networks is essential in various fields, encompassing soft matter science and engineering (such as studying the rheological behaviors of colloidal gels and emulsions with applications in cosmetics [13], paints [14,15], drilling [7], and foods [16]), materials science (for the development of advanced materials with tailored mechanical properties such as fuel cells [17,18]), biophysics and bioengineering (to investigate the mechanical response of biological tissues, cellular aggregates, and biomaterials [19,20]), geology and geotechnical engineering (for assessing the stability of soil and rock network structures [21,22]), and granular materials and powders (to understand the compaction of wet granular materials like soils and grains [22,23]). Despite the importance of these phenomena in natural and industrial contexts, the relationship between network microstructure and compressive yielding remains poorly understood.

The mechanical stability of colloidal gels against gravity is a critical issue in this context. Gels are formed through arrested phase separation of colloidal suspensions, resulting

*tanaka@iis.u-tokyo.ac.jp

in a percolated network that imparts macroscopic elasticity and enables them to resist gravitational stress [1,2,24]. However, due to the intrinsic nonequilibrium nature of gels, their mechanical properties change slowly over time as their microstructure evolves. When the gravitational stress exceeds the gel's yield stress, the gel collapses, a process that has garnered considerable attention and has been extensively studied due to its fundamental and practical importance [2,6,25–37]. The collapsing behavior depends on the initial volume fraction $\phi_{\rm init}$ and the scaled temperature $k_{\rm B}T/\epsilon$ ($\epsilon$ and $k_{\rm B}$ being the attraction strength and the Boltzmann constant, respectively). It can be classified into rapid, delayed, or creeping collapses [25,26,34,36]. These complex collapse patterns indicate the dynamic interplay between aging-induced temporal changes in the gel's structure and the yielding process. Various interesting behaviors have been observed in the aging regime, such as network rupture [32,33], volume-fraction increase at the top layer of gels [36], and coarsening of network arms driven by osmotic pressure [6].

Experimentally, the dynamical processes during gravitational compression have been intensively studied through macroscopic observations, such as monitoring the temporal change of the top surface position of a gel, and height-resolved observations, such as measuring the height-resolved volume fraction $\phi(z,t)$ and sedimentation velocity $u_z(z,t)$, where $z$ is the height. These studies have partially supported the validity of a coarse-grained poroelastic model [38–40], especially for the rapid collapse case. However, the constitutive equation for the yield stress and solvent permeability through a network lacks a microscopic foundation, which hinders a full understanding of the underlying physics.

The yield stress of a gel $\sigma_{zz}$ has been accessed by measuring the volume-fraction profile at the final settled state $\phi_{\rm eq}(z)$, assuming the mechanical equilibrium condition, $\partial_z\sigma_{zz} + \Delta\rho g\phi_{\rm eq} = 0$, where $g$ and $\Delta\rho$ are the gravitational acceleration and mass-density difference between colloids and solvent, respectively [31,41–44]. Interestingly, these studies have reported that the yield stress $\sigma_{zz}$ is determined by $k_{\rm B}T/\epsilon$ alone, independent of $\phi_{\rm init}$ [31,41–44]. Furthermore, nontrivial scaling of $\sigma_{zz}$ for various $k_{\rm B}T/\epsilon$ [41,43,44] and a crossover from power-law to divergent growth of $\sigma_{zz}$ toward the random close packing volume fraction $\phi_{\rm RCP}$ have also been observed [41,44]. However, the microstructural evolution of gels under stress and its connection to the yield stress remain unclear since previous studies have relied on observations of final mechanical equilibrium gels after complete collapse.

In this study, we employ real-time *in situ* three-dimensional (3D) confocal microscopy at a single-particle level to observe the gravitational collapsing process of colloidal gels. As emphasized above, the structural changes in gels are driven by both external mechanical stress and aging effects. For systematically studying the microstructural evolution of gels during yielding, it is essential to isolate the collapsing process from the aging process. To achieve this, we employ a specially designed cell capable of promptly applying buoyancy to well-aged gels prepared without subjecting them to gravitational stress. This approach enables us to track the particle-level structural evolution of a gel with a well-defined initial structure during sedimentation, free from aging effects. By manipulating gravitational force, we have effectively investigated the relationship between the gel's microstructural evolution and its mechanical yielding under low strain rates. Additionally, to obtain information on the mechanical stress, we have conducted Brownian dynamics simulations for gravitational collapse and homogeneous uniaxial compression. Through comparisons with these simulation results, we have also verified that the experimental results reported below can be considered quasistatic.

Despite substantial changes in the microstructure of the gel during gravitational collapse, we have discovered that, throughout the collapsing process, the microstructural characteristics, such as the average coordination number and characteristic pore size, are statistically uniquely determined by the local volume fraction $\phi$ alone. This relationship remains independent of the deformation strain history the system experienced but is subtly influenced by the preparation history of the initial conditions, characterized by the volume fraction $\phi_{\rm init}$ and the age $t_{\rm age}$ of the gel's initial state. On the other hand, the compressive stress adheres to a distinct function determined solely by the local volume fraction during compression, except during the initial transient behavior (e.g., stress overshoot). This function remains unaffected by both the preparation and strain histories, as long as the interparticle interaction is identical. Furthermore, we observed two distinct microstructural changes during the compression process: the emergence of compact clusters experiencing significant strain and undergoing yielding, and the formation of chainlike structures along the compressive axis that support external stress. Our findings indicate that the gel's microstructure mechanically self-organizes into a unique history-independent absorbing state solely determined by the volume fraction under external compressive stress.

## II. METHODS

### A. Experiments

Here, we describe a unique experimental protocol using a custom-made cell that allows us to observe the gel's gravitational collapse process without the influence of the aging effect. We first prepare a density and refractive-index matched colloidal suspension of diameter $a = 1.9$ μm of the volume fraction $\phi_{\rm init} = 0.19 \pm 0.01$, including polymers (the concentration $C_{\rm p}$) but no salt, in a sample chamber (see Appendix A and Fig. 7 in Appendix B for the details on the sample and the sample cell, respectively).

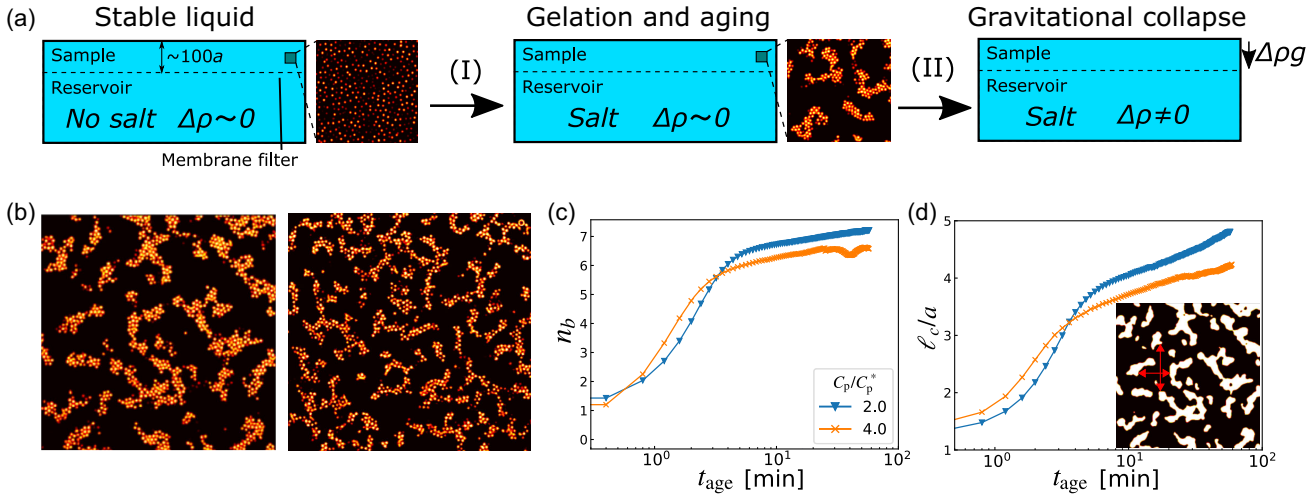


FIG. 1. Experimental protocol and results of colloidal gelation. (a) Schematic figure of a sample cell used in our experiment. Colloids in the sample chamber are density matched to create a stable homogeneous liquid state (left). Then, we replace the solvent in the reservoir chamber with the one with salt (I). This quickly screens intercolloid electrostatic repulsion through ion diffusion across a semipermeable membrane, which activates polymer-induced depletion attractions between colloids and initiates colloidal phase separation and gelation (middle). After forming the gel, we replace the reservoir solvent with the one without density match with colloids (II) to induce the colloids' buoyancy and initiate the colloidal gel's gravitational collapse (right). (b) 2D confocal $xy$-slice images for colloidal gels with $C_p/C_p^* = 2$ (left) and 4 (right) at the final frame of observation of the gelation dynamics. (c),(d) The time evolution of the average coordination number per particle $n_b$ and characteristic pore size $\ell_c$ during gelation, respectively. The inset in (d) is a binarized image of the left-hand side of (b), where the white and black regions correspond to the colloid network and pores, respectively.

In this stage, colloids are homogeneously dispersed free from aggregation due to the intercolloid Coulomb repulsion [left-hand panel in Fig. 1(a)]. Then, we introduce a solvent with both polymers (the same concentration as in the sample) and salt into a reservoir chamber [see protocol (I) in Fig. 1(a)], which is in contact with the sample chamber through a semipermeable membrane. The salt quickly diffuses into the sample chamber through the membrane, screens the Coulomb repulsion, and makes the polymer-induced depletion attraction between colloids active (the attraction range $\Delta \sim 0.13$; see Appendix A for details), initiating phase separation of the colloidal suspension into the colloid-rich and -poor phases. This allows us to observe the gelation dynamics from the beginning and prepare an ideal colloidal gel state without any mechanical and hydrodynamic perturbations [the middle panel in Fig. 1(a)]. See Refs. [45–47] for the details and validity of this method.

After forming the gels, we replace the reservoir solvent with the one without density match with colloids ($\Delta\rho \neq 0$) to induce the colloids' buoyancy $F_g = \pi a^3 \Delta\rho g/6$ and initiate the gravitational collapse of colloidal gels [see protocol (II) in Fig. 1(a)]. We set the gravitational Péclet numbers to be $\mathrm{Pe} = F_g a/2k_B T = 0.16, 0.32, -0.32$. The positive and negative Pe's correspond to the floating and sedimentation of gels (see Appendix B for further details), and we orient $z$ coordinate such that the buoyant force points toward $-z$. Here, it is worth noting that the comparisons with numerical simulation results below demonstrate that the processes under investigation can be regarded as quasistatic. By combining this protocol with high-precision dynamical particle tracking (see Figs. 8 and 9 and Appendix C), we investigate the gravitational collapsing of a gel with single-particle resolution.

In Fig. 1(b), we show 2D confocal images of the two gel states formed by protocol (I) for $C_p/C_p^* = 2$ and 4, where $C_p^* = 0.25$ g/L is the critical polymer concentration above which colloids aggregate. The waiting times from the initiation of gelation (~1 h), or the age of the gels, correspond to $t_{age} \simeq 1500$ and 1100 in the unit of the Brownian time $\tau_B = (a/2)^2/6D_0$ ($D_0$ is the diffusion constant of a free particle) for the gels of $C_p/C_p^* = 2$ and 4, respectively. To characterize the gelation processes reaching these final states at the microscopic level, we follow the temporal change of the average coordination number $n_b$ (the number of interparticle bonds per particle; see Appendix D for the details), as shown in Fig. 1(c). Initially, $n_b$ experiences a rapid increase, but its growth significantly slows down as it approaches Maxwell's isostaticity criterion ($2d = 6$, where $d$ is the dimensionality). This observation supports the notion that the dynamic slowing down in the gelation of colloids with short-range attractions is caused by the percolation of mechanically rigid particles [8,45,47–49]. To see the structural evolution in a different length scale, we monitor the temporal change of the characteristic pore size $\ell_c$ obtained as the mean value of the chord length distribution $P(\ell)$ (see Appendix D), as shown in Fig. 1(d). $\ell_c$ increases

in the early stage but shows a logarithmic growth in the late stage, similarly to $n_b$. Furthermore, by comparing $n_b$ and $\ell_c$ for the two different $C_p$'s, we find a notable difference in the gel structure between them; the network formed at the larger $C_p$ has thinner strands and smaller pore sizes than the one at the smaller $C_p$ [see Fig. 1(b)]. Below, we show that such a difference in $C_p$ (or $\epsilon/k_BT$ in simulations) significantly impacts the dynamic route of the gravitational collapse.

### B. Simulations

We perform the Brownian dynamic simulation using the LAMMPS package. The short-range depletion attraction between colloids is modeled using the Morse potential, $U(r) = \epsilon(e^{2\rho(a-r)} - 2e^{\rho(a-r)})$, where $\rho a$ is set as 48.63 to match the attraction range in the experiments ($\Delta = 0.13$) [46] and a linear correction term is added to truncate $U$ at $r/a = 1 + \Delta$ smoothly (i.e., $U = U' = 0$). The position $\boldsymbol{R}_i(t)$ and the velocity $\boldsymbol{V}_i(t)$ for particle $i$ ($i = 1, 2, \ldots, N$) obey the following overdamped Langevin equation: $d\boldsymbol{R}_i(t)/dt = \boldsymbol{V}_i(t) = \zeta^{-1}(\boldsymbol{F}_i + \boldsymbol{F}_i^{\mathrm{R}})$. Here, $\boldsymbol{F}_i = -\sum_j (\partial/\partial \boldsymbol{R}_i) U(|\boldsymbol{R}_j - \boldsymbol{R}_i|)$ is the force acting on particle $i$, $\zeta$ is the viscous friction constant, and $\boldsymbol{F}_i^{\mathrm{R}}$ is the random force, which satisfies the following fluctuation-dissipation relation: $\langle \boldsymbol{F}_i^{\mathrm{R}} \rangle = \boldsymbol{0}$ and $\langle F_{i\alpha}^{\mathrm{R}}(t) F_{j\beta}^{\mathrm{R}}(t') \rangle = 2k_{\mathrm{B}}T\zeta\delta_{ij}\delta_{\alpha\beta}\delta(t-t')$.

This simulation method does not account for many-body hydrodynamic interactions (HIs), which arise from the dynamic coupling between colloidal and solvent motions. However, we have confirmed that the impact of HIs on the final structure of the gel at $\phi_{\mathrm{init}} = 0.2$ [$t/\tau_{\mathrm{B}} \sim \mathcal{O}(10^3)$] is minimal [50], although the aggregation process preceding gelation [$t/\tau_{\mathrm{B}} \lesssim \mathcal{O}(10^2)$] is significantly influenced by HIs [46]. In Fig. 10 and Appendix E, we demonstrate that, for the small Pe's employed in our study, HIs play a minor role in the gel's microstructure during gravitational collapse. It is noteworthy that HIs influence the sedimentation speed of the system, although this does not affect the analysis results presented in the main text.

We scale the above equation of motion using $a$ and $a^2\zeta/\epsilon$ as the length and time units, respectively, and integrate it under the Euler scheme with a time step $\Delta t = 1.0 \times 10^{-5}$. To characterize the strength of intercolloid attraction and buoyancy, we use the scaled temperature $\hat{T} = k_{\mathrm{B}}T/\epsilon$ and $\hat{F}_g = F_g a/\epsilon$, respectively. Then, the experimental parameters $C_{\mathrm{p}}/C_{\mathrm{p}}^* = 2$ and 4 approximately correspond to $\hat{T} = 0.143$ and 0.071, and $\mathrm{Pe} = 0.16$ and 0.32 correspond to $\hat{F}_g = 0.0432$ and 0.0864. Hereafter, we omit the scaling symbol "$\hat{}$" to avoid cumbersomeness.

To prepare the initial conditions, we first equilibrate the system at a high temperature ($T = 1$) and then drop the temperature to obtain arrested gels (the scaled waiting time being $t_{\mathrm{age}} = 3000\tau_{\mathrm{B}}$). Then, we add a constant external force $-F_g\boldsymbol{e}_z$ on all particles along the $z$ direction, to see the dynamical processes of gravitational collapse. Here, we introduce two flat walls perpendicular to $z$ axis, with a gap of $L_z = 100a$, and impose the periodic boundary condition in $x$, $y$ directions (the system size is $L_x = L_y = 34.6a$). The walls interact with particles through the above Morse potential during the gelation processes, but we remove the interaction with the upper wall during the sedimentation processes to avoid complex behavior such as network detachment from the top wall.

Additionally, to observe the compression behavior without global density gradient along $z$ axis, we perform uniaxial compression simulations under periodic boundary conditions in all directions. In each step, we first update the particle positions by integrating the above overdamped Langevin equation. Subsequently, we change the system size and particle positions along the $z$ axis with a constant deformation rate of $\kappa = -6.93 \times 10^{-4}$. Specifically, we update the $L_z$ (and $R_{i,z}$) as $L_z(t + \Delta t) = L_z(t)\exp(\kappa\Delta t)$, where $L_z(0) = 2L_x$, $L_x$ and $L_y$ fixed at $34.6a$. We continue the compression until $L_z$ reaches $L_x$. It is important to note that this algorithm ensures that the rate of instantaneous strain, $[L_z(t_1 + t_0) - L_z(t_0)]/L_z(t_0) \simeq -[\phi(t_1 + t_0) - \phi(t_0)]/\phi(t_0)$ ($t_0$, reference time; $t_1$, interval from $t_0$), is constant ($\kappa$) for small $t_1$. We compared the results obtained at a rate of $-6.93 \times 10^{-5}$ for the volume fractions within our range of interest ($0.2 \le \phi \le 0.6$), and we did not observe any significant differences. Based on this analysis, we can conclude that our compression simulations can be considered practically quasistatic. By employing these simulations with sufficiently slow deformation rates, we can effectively prevent density inhomogeneity along the compression direction (see Fig. 11 and Appendix F for the detailed discussion on the uniformity of the volume-fraction profile). This simplifies the interpretation of the results to a great extent, enabling a clearer understanding of compressive yielding.

## III. RESULTS

### A. Gravity-induced compression of colloidal gels

Using the gels obtained from protocol (I) as the initial states, we impose the gravitational force on colloids by quickly switching on the buoyancy force $F_g$, i.e., by replacing the existing density-matched solvent in the reservoir chamber with a solvent with a targeted density mismatch $\Delta\rho$ [see protocol (II) in Fig. 1(a)]. Note that the refractive index of the solvents is kept matched between the two solvents (see Appendix A); therefore, the intercolloid interaction is unchanged by this solvent exchange. We set the gravitational Péclet numbers to be $\mathrm{Pe} = 0.16$, 0.32 (floating) and $-0.32$ (sedimentation), which are strong enough to induce the gravitational collapse of gels [51].

Here, we emphasize that the gels discussed in our study are physical colloidal gels, formed through the dynamic

arrest of network-forming phase separation. Such gels constitute an entirely distinct material category compared to chemical colloidal gels, which are particle networks stabilized by chemical interactions between the surfaces of colloids [1,2]. Notably, physical gels lack a fractal microstructure and a restoring force for bond-bending, characteristics present in chemical gels. Refer to, for example, Refs. [52–58] for studies on the compression or sedimentation of chemical gels.

Under the above conditions, the collapse starts immediately after the solvent replacement (within 1–2 min); see Supplemental Material, Movie 1 [59]. The time window of the collapse observation (∼2 h) is in the same order as $t_{\mathrm{age}}$. Since the aging proceeds logarithmically, it has little impact in this timescale. Therefore, unlike previous experimental studies, we can follow structural changes driven by gravitational stress alone, free from the aging effects. To our best knowledge, our work is also the first particle-level 3D observation for the gravitational collapse of colloidal gels, although several earlier studies observed $xz$ cross sections of colloidal gels with confocal microscopy [28,32,34,37].

We first provide an overview of the collapse process and examine if our results reproduce the previous studies. Hereafter, we mainly focus on the results for $(C_{\mathrm{p}}/C_{\mathrm{p}}^{*}, \mathrm{Pe}) = (2, 0.32)$; the results for other trajectories are provided in Fig. 14 of Appendix I. Figure 2(a) shows 3D reconstructions of the confocal images for a collapsing gel, which cover from the top to the bottom layers of the sample chamber (the width being $90a$–$100a$), together with the $xy$-slice images (the size being $56^2a^2$) at the bottom of the sample chamber. We can see that the particle density at the bottom increases as the gel collapses (see also Supplemental Material Movie 1 [59]). This behavior can be characterized quantitatively by following the time evolution of the volume-fraction profile $\phi(z,t)$ [see Fig. 2(b)] [refer to Appendix D for the method of computing $\phi(z)$]. Note that the peak in the $\phi(z)$ profile develops slightly above the bottom wall of the sample chamber (see the vertical dashed line in the figure) due to the density depletion near the sample walls at the initial state.

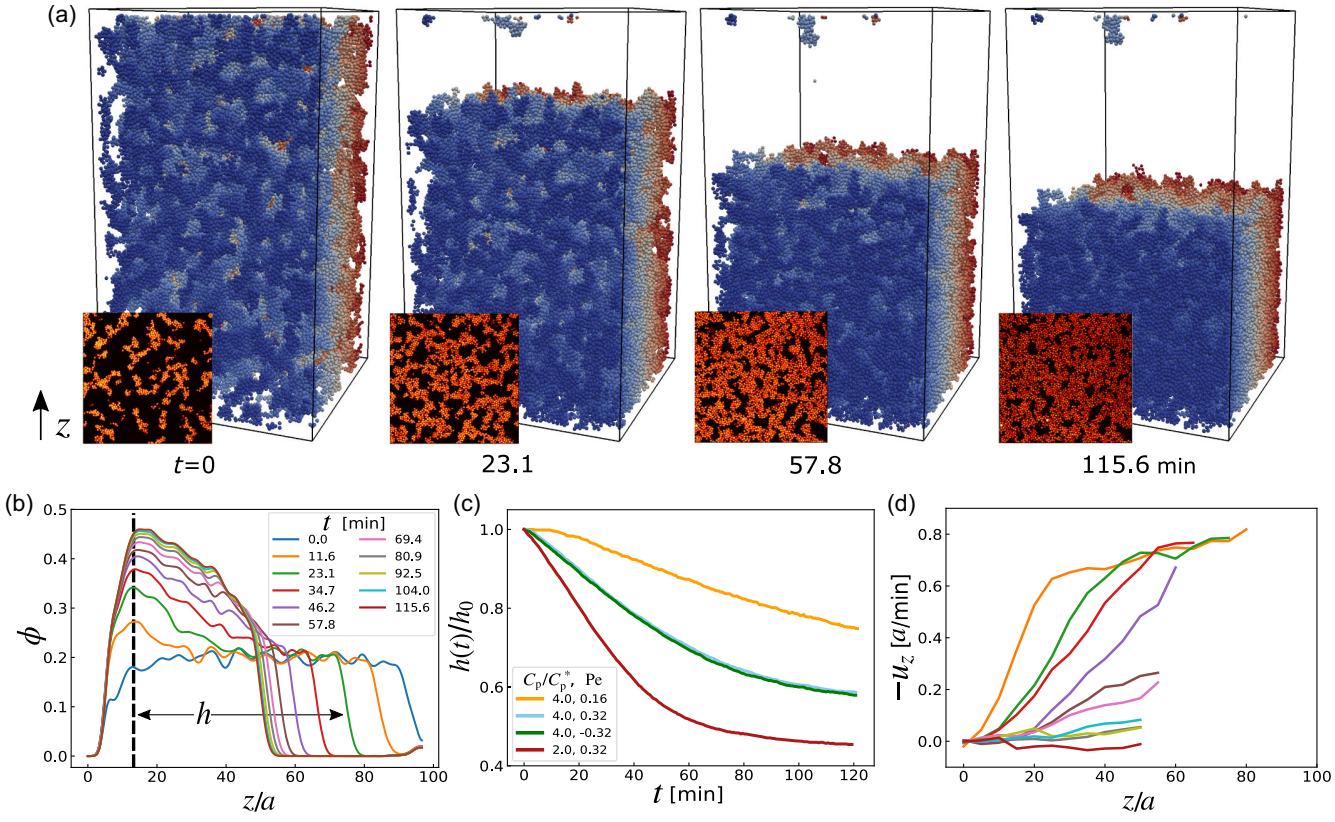


FIG. 2. 3D observation of the gravitational collapse of a colloidal gel with confocal microscopy. (a) 3D reconstruction of a confocal image for the collapsing gel at a different time (see also Supplemental Material Movie 1 [59]). Particles are colored to distinguish the front from the back. We also show the confocal 2D image of the sample chamber's bottom in the $xy$ plane [at the location of the vertical dashed line in (b)]. (b) The volume-fraction profile $\phi(z)$ as a function of height $z$ and elapsed time $t$. (c) The time evolution of the front position, i.e., the distance from the sample chamber's bottom to the front of the collapsing gel $h$ [see the black arrow in (b)], for various trajectories. Here, we scale $h$ by its initial value $h_0$ at $t = 0$ min. (d) The $z$ component of the average colloid velocity $u_z(z,t)$, estimated from the particle displacements between two subsequent times (the time interval $\Delta t = 0.68$ min). Panels (b) and (d) correspond to the results for $(C_{\mathrm{p}}/C_{\mathrm{p}}^{*}, \mathrm{Pe}) = (2, 0.32)$, and those for other trajectories are shown in Fig. 14 of Appendix I.

The deposition of particles on the walls in the early gelation stage may create this depleted region.

We regard the peak position of $\phi(z)$ as the bottom of the collapsing colloidal gel and measure the gel height $h$ from this bottom to the gel's top surface as a function of time; the result is shown in Fig. 2(c). We can see that $h$ decreases faster, and its final gel height $h$ is smaller for weaker intercolloid interaction and stronger gravitational strength. The collapsing speed, i.e., the slope of $h(t)$ around $t = 0$, is not maximum, unlike several previous studies (see, e.g., Refs. [34,36]), which may be because the detachment of the gel network from the top wall of the sample chamber retards the collapse process. We can also see that the direction of buoyancy, sedimentation (green curve) or floating (blue curve), has little influence on the behavior as long as the magnitude is the same. The excellent agreement between the two curves also shows the robustness of our experimental method.

Figure 2(d) shows the $z$ component of the average colloid velocity, $u_z(z,t)$, obtained from the displacements of particles between two subsequent times ($\Delta t = 0.68$ min; see Appendix C regarding how to construct the particle trajectories). In the early stage, the sample can be divided into the free-falling supernatant part with little deformation (the $z$ region with constant $\phi$) and the lower part under significant deformation (the $z$ region where $\phi$ increases with decreasing $z$). However, the supernatant part disappears in the late stage ($t \gtrsim 46.2$ min). These two distinct time regimes correspond to the linearly decreasing behavior and the subsequent nonlinear saturation of $h(t)$ [Fig. 2(c)]. This behavior of $h(t)$ is similar to typical behaviors observed in the rapid collapse but different from the delayed collapse or creeping-type collapse (see, e.g., Refs. [33,34,36]). This is natural since the delayed and creeping-type collapse cases are much more seriously affected by the gel's aging than the rapid collapse case. This observation supports that the collapsing process of the gel is free from aging effects.

### B. Absorption into a history-independent state

Now, we examine the microstructural evolution of the collapsing gels under gravity. To systematically evaluate the influence of the evolution of $\phi(z,t)$, we divide the entire system into layers with a width of $3.5a$ along the $z$ axis and measure $\phi(z)$, $n_b(z)$, and $\ell_c(z)$ layer by layer as a function of time $t$. The bin size of the layers is chosen to be sufficiently large to conduct structural analysis with statistical significance and small enough to ensure that the variation in $\phi(z)$ within the layer is effectively negligible [see Fig. 2(b) and also Fig. 14 in Appendix I]. Note that we measure $\ell_c$ only in the $xy$ plane since the system is subject to strong $\phi$ gradient along the $z$ axis at the pore-size scale. Figures 3(a) and 3(b) show the mappings of $\phi$-$n_b$ and $\phi$-$\ell_c$, respectively, for four different trajectories. Notably, the data for different $z$, $t$, and Pe collapse onto the same curve. This result suggests that while the microscopic structure of collapsing gels exhibits strong heterogeneity depending on height and elapsed time, the network structure of the gel undergoing collapse is statistically determined solely by the local volume fraction $\phi$ measured in each layer at a given height $z$. In other words, the microstructure evolves as a function of $\phi$, independent of the strain history that the system has experienced.

This phenomenon of colloidal gels being absorbed into a unique state under external stress somewhat resembles the critical steady state observed in dense amorphous solids under unidirectional shear deformation [12,60]. Additionally, another type of absorbing state transition has been observed in non-Brownian suspensions [61,62] and granular materials [63,64] subjected to cyclic shear. However, a critical difference is that in our case, as the volume fraction increases with compression, the absorbing state undergoes continuous changes rather than remaining steady. It is also crucial to note that this history-independent state is unique to compressive yielding and significantly differs from behaviors observed in shear-induced yielding of colloidal gels. In shear-induced yielding, unidirectional shear leads to global-scale network rupture, whereas oscillatory shear results in the slow coarsening of network strands (see, e.g., Refs. [7,10,11]).

The failure of data collapse for different $C_p$ implies that the state to which the system is absorbed depends on the attraction strength $\epsilon/k_BT$. In Fig. 3(c), we present the chord length distributions $P(\ell)$ for the same volume fraction but at different times (the corresponding simulation results are provided in Fig. 15 and Appendix I). The data collapse of $P(\ell)$ for a given $\phi$ further confirms the existence of the history-independent state unique to compressive yielding. We verify that the same trend holds for the number density of local structures identified by topological cluster classification [2,23,65,66] [see Figs. 12(a)–12(c) and Appendix G].

Then, a critical question is how this structural feature relates to mechanical properties. In the experiments, it is difficult to obtain information on intercolloid forces (the attraction range being $0.13a$) due to the limited accuracy of particle tracking (roughly 200 nm $\simeq 0.1a$). We mention that an experimental setup using special emulsions to estimate interparticle forces from confocal images has been developed recently [67]. Here, we consider results obtained from Brownian dynamics simulations of gel collapsing and compare them with the above experimental results by matching the initial condition of gels, i.e., ($\epsilon/k_BT$, $\phi_{\mathrm{init}}$, $t_{\mathrm{age}}$) between the experiments and simulations (see Sec. II B for the details).

The triangle and cross symbols in Figs. 3(d) and 3(e) show the mapping of $\phi$-$n_b$ and $\phi$-$\ell_c$, obtained from the simulation results of gravitational collapse, reproducing the essential features of the corresponding experimental results in Figs. 3(a) and 3(b). In Fig. 10 and Appendix E, we confirm that these microstructural signatures remain

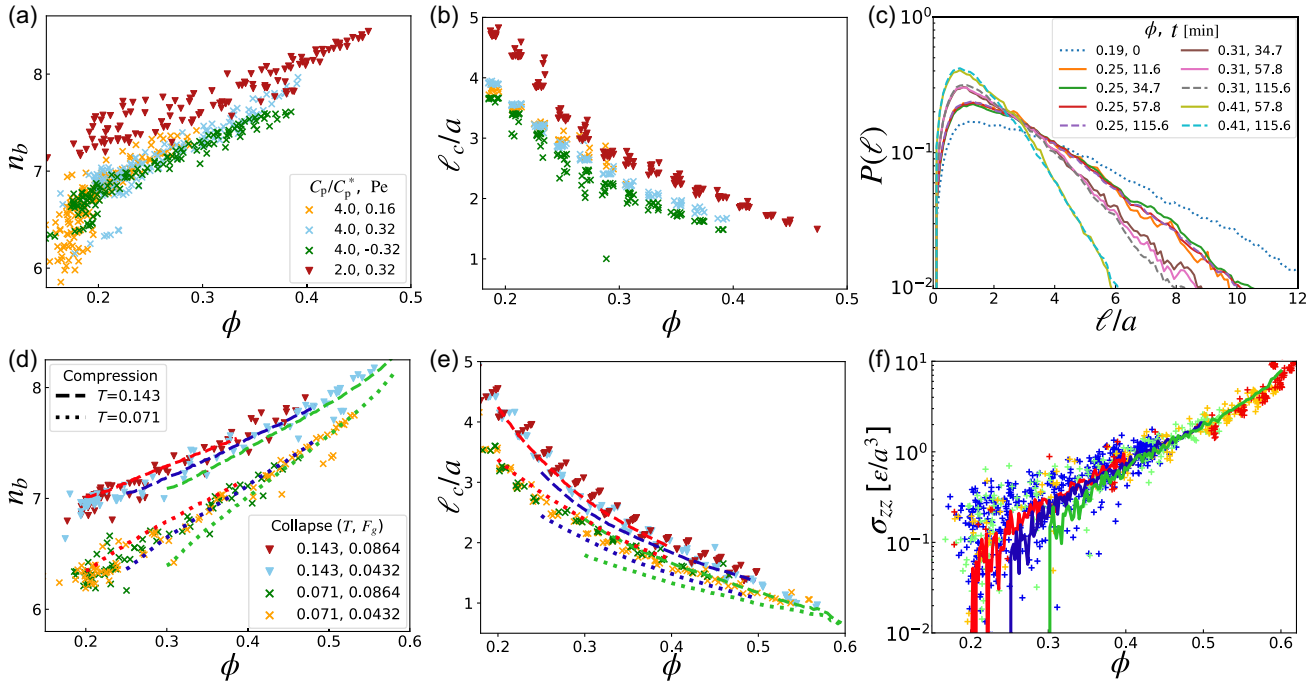


FIG. 3. Comparison of gel's microstructure during compressive yielding between experiments and simulations. (a)–(c) Experimental results. (a) The average coordination number per particle $n_b$ for various $z$ and $t$. (b) The characteristic pore size $\ell_c$ along the $xy$ plane for various $z$ and $t$. The brown cross, blue cross, green cross, and red triangle symbols in (a) and (b) represent the trajectory at $(C_p/C_p^*, \mathrm{Pe}) = (4, 0.16)$, $(4, 0.32)$, $(4, -0.32)$, and $(2, 0.16)$, respectively. (c) Comparison of the chord length distribution $P(\ell)$ under fixed volume fractions ($\phi = 0.25, 0.31, 0.41$) between the intermediate (solid lines, $t = 13.6, 34, 68$ min) and late time (dashed lines, $t = 115.6$ min). The dotted line represents $P(\ell)$ for the initial condition. Here we show the result for $(C_p/C_p^*, \mathrm{Pe}) = (2, 0.32)$. (d)–(f) Simulation results. (d),(e) $\phi$ dependence of the average coordination number per particle $n_b$ and the characteristic pore size $\ell_c$, respectively. Triangle and cross symbols are the results of the gravitational collapse at $T = 0.071, 0.143$ and $F_g = 0.0432, 0.0864$, for which we start the simulation with the same volume fraction $\phi_{\mathrm{init}} = 0.2$. Dotted and dashed lines are the results of uniaxial compression at $T = 0.071, 0.143$, respectively. Here, we show the results from three different initial conditions: $\phi_{\mathrm{init}} = 0.2$ (red), 0.25 (blue), 0.3 (green). (f) $\phi$ dependence of stress $\sigma_{zz}$ at $T = 0.071$. Cross symbols are the results of gravitational collapse simulations. Each cross symbol corresponds to a map of $(\phi, \sigma_{zz})$ for a given pair of $(z, t)$. The color indicates the gravitational strength: $F_g = 0.043$ (blue), 0.086 (green), 0.173 (brown), and 0.345 (red). Solid lines are the results of uniaxial compression for three different initial conditions: $\phi_{\mathrm{init}} = 0.2$ (red), 0.25 (blue), and 0.3 (green).

unaffected by the presence or absence of hydrodynamic interactions, while HIs significantly affect the sedimentation speed. To see the relationship between the structure and mechanics, we evaluate the volume-fraction dependence of the stress $\sigma_{zz}$ following the expression of the virial stress; the results are shown in Fig. 3(f). Each point in the figure corresponds to a pair of $(\phi, \sigma_{zz})$ measured for each layer at height $z$ and elapsed time $t$, and the colors of the points are labeled following the value of $F_g$.

On the other hand, the red line in Figs. 3(d)–3(f) represents the same result but obtained from simulations of homogeneous uniaxial compression (along the $z$ axis), which coincides well with the curves for gravitational collapse. This indicates that the system has been mechanically self-organized into a unique history-independent state after a short period of transient behavior (see also Fig. 16 in Appendix I), irrespective of the presence or absence of the spatial gradient of the volume fraction $\phi$ as well as the height of the initial gels $h_0$.

Here, it is worth stressing that the global strain rate in uniaxial compression simulations is sufficiently low (see Sec. II B for the detail). Hence, the observed yielding behavior can be practically regarded as quasistatic. This indicates that the unique state in compressive processes is characterized by a low strain rate, ensuring that it evolves in a manner that maintains mechanical balance. This observation also explains why the microstructure of the gel is little affected by the presence or absence of hydrodynamic interactions (see Fig. 10 and Appendix E). Furthermore, the persistence of the $\sigma_{zz}$-$\phi$ relation, unaffected by volume fraction gradients along the compression axis, emphasizes the local nature of the mechanical equilibrium (see also Appendix F).

### C. Structure and stress dependence on the preparation history of the initial states

Next, we consider how the structure and stress evolution depends on initial conditions. The blue and green lines in

Fig. 3(f) represent the stress $\sigma_{zz}$ for initial volume fractions different from the one in gravitational collapse ($\phi_{\rm init} = 0.25,\ 0.3$). All the points from the gravitational collapse simulations and the lines from uniaxial compression simulations are absorbed onto a single master curve, implying the uniqueness of the stress for a given $\phi$. Such a link of the macroscopic stress to the volume fraction has been assumed in a standard coarse-grained model [38–40]. Our results establish that $\sigma_{zz}(\phi)$ is unique even if the compressive yielding process is ongoing when the strain rate is sufficiently low, providing the first microscopic support for this hypothesis. Note that the transient behavior of $\sigma_{zz}$ before entering into the history-independent state exhibits either ductile (overshoot) or liquidlike (monotonic increase) fractures, depending on the preparation protocol of initial conditions [see Figs. 13(c) and also 16 in Appendix I for the shape of $\sigma_{zz}(\phi)$ under the other parameter settings], as observed in the case of shear yielding of dense amorphous solids [12].

In our study, we denote the stress $\sigma_{zz}(\phi)$ in this absorbing state as the yield stress. It is important to note that while this notation is consistent with earlier studies on the compressive yielding of colloidal gels (see Sec. I), in yielding phenomena of amorphous dense solids under unidirectional shear, the yield stress is often defined as the maximum stress in the stress overshoot that appears before reaching the critical steady state [12,60]. Under substantial gravitational stress, the layer at the bottom of the sample chamber can reach a very dense state with few pores, crossing over from heterogeneous gels to homogeneous attractive glasses. This structural homogenization is accompanied by the sharp increase of the yield stress toward $\phi_{\rm RCP}$ [41,44].

In Figs. 3(d) and 3(e), we can see that the collapse and compression simulations yield almost exactly identical behavior for the same $\phi_{\rm init}(= 0.2)$. However, slight mismatches in structural evolution are noticeable among different $\phi_{\rm init}$ values, even in the late stages. This suggests that while $\sigma_{zz}$ at fixed $\phi$ is common for different $\phi_{\rm init}$, their microstructures are not strictly identical, albeit very similar.

To further investigate this point, we monitor the evolution of local structures for different $\phi_{\rm init}$ values and find that the number densities of the tetrahedral (three-ring) structures and pentagonal pyramid (five-ring) structures follow master curves, while that for square pyramid (four-ring) structures does not [see Fig. 12(d) and Appendix G], indicating the presence of relevant and irrelevant structures in the compressive yielding process. In Fig. 13 and Appendix H, we examine $t_{\rm age}$ dependence (which covers two decades) on the evolution of $n_b$, $\ell_c$, and $\sigma_{zz}$ under uniaxial compression, and the role of $t_{\rm age}$ is essentially the same as that of $\phi_{\rm init}$: $t_{\rm age}$ alters the structural evolution slightly, whereas it does not affect the stress evolution except during the early transient stage.

### D. Microstructures characteristic of particles exhibiting high strain and stress

In the above, we have seen that in actual gel's structure, the preparation history of the initial conditions ($\phi_{\rm init}$ and $t_{\rm age}$) are mostly erased during compression, but not completely. In contrast, the stress is not influenced by the preparation protocol of gels, i.e., the initial conditions, except during the initial transient stage. Then, a question that naturally arises is what kind of microscopic structure or dynamics in the history-independent state is linked to the global-scale deformation and magnitude of yield stress. To address this question, we first examine if there is an experimental signature that can characterize the yielding process. As a typical indicator of microscopic structural changes, we monitor the particle-level shear strain $\gamma$, following Ref. [68] (see Appendix D). The distributions of shear strain $P(\gamma)$ for different reference times $t_0$ are shown in Fig. 4(a), where the time interval is the one between two subsequent frames ($\Delta t = 0.68$ min). Here, we find that $P(\gamma)$ has a peak around $\gamma \sim 0.05$ with an exponential tail in the high $\gamma$ side. Additionally, in Fig. 4(b), we show a snapshot of particles belonging to the tail part ($\gamma > 0.2$). We can see that particles subjected to large deformation form small compact clusters (see also Movie 2 in Supplemental Material [59]). These results indicate that the network structure almost retains its shape during sedimentation to keep mechanical balance and that the localized structural changes involving a tiny number of particles are responsible for the global yielding.

To access the purely mechanical features, next we examine the simulation results for uniaxial compression at zero temperature, where the influence of thermal noise and volume-fraction gradient along the $z$ axis (at the pore-size scale) are absent (see Appendix F). We confirm the absorption into a history-independent state in this condition (see Fig. 16 and Appendix I). We identify the top 10% of particles with high particle stress $\sigma_{zz}$ and strain $\gamma$, and

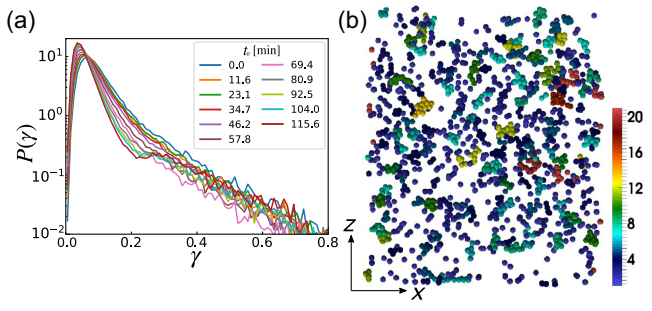


FIG. 4. Microscopic yielding process observed in experiments at $(C_{\rm p}/C_{\rm p}^*, {\rm Pe}) = (2, 0.32)$. (a) The distribution of microscopic shear strain $\gamma$ for various reference time $t_0$ (see the legends) and time interval of $\Delta t = 0.68$ min. (b) Visualization of highly strained particles ($\gamma > 0.2$) at $t_0 = 46.2$ min. The color indicates the size of the clusters to which each particle belongs. See also Supplemental Material Movie 2 [59].

perform a structural analysis of the corresponding clusters identified by using the interaction range as a threshold. Figures 5(a) and 5(b) show the snapshots of the top 10% particles with high strain and stress, respectively. In Fig. 5(c), we show the relationship between the number of particles belonging to each cluster $N$ and its gyration radius $R_g$ for the top 10% strained and stressed particles. The power exponent $d_f$ in the equation $R_g^{d_f} \propto N$, known as the fractal dimension, characterizes the morphology of the clusters. Statistically, the top 10% strained particles form spherical clusters with $d_f \sim 3$, whereas the clusters of the top 10% stressed particles exhibit a more chainlike structure with $d_f \sim 1.5$. These structural features can also be directly observed from the real-space structures of these particles shown in Figs. 5(a) and 5(b). Movie 3 in Supplemental Material demonstrates that these trends are commonly observed during compression at finite temperatures [59].

Figure 5(d) shows the fractions of ruptured bonds for these two types of clusters and all bonds. The bonds in stressed clusters are more compression resistant than the others, indicating that highly stressed structures are more likely to survive during compression and grow selectively under compression. It is worth noting that the size of compact strained clusters seen in Fig. 5(a) is typically comparable to the network or strand width, which is a few particle diameters. This trend is markedly different from the shear yielding of jammed systems, where a system-spanning shear band is formed [12,69]. Furthermore, as illustrated in Fig. 5(a) (see also Supplemental Material Movie 4 [59]), there is little spatial correlation between the formed (green) and ruptured (red) bonds. This indicates that $T1$ events are minor in the compressive yielding of an inhomogeneous colloidal gel, unlike in homogeneous jammed systems [70] and glass systems [68]. It is intriguing how the microscopic yielding behavior changes with increasing the volume fraction across the gel-to-glass crossover.

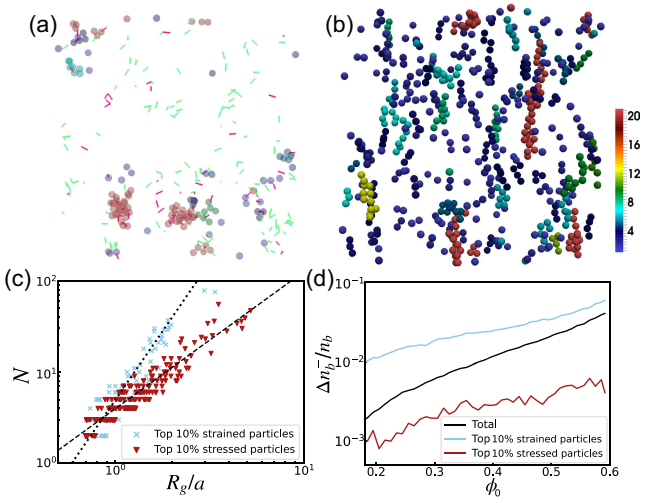


FIG. 5. Microscopic mechanically relevant structures in uniaxial compression simulations. (a) The top 10% particles with high particle shear strain $\gamma$. The red and green bars are the bonds that rupture and form by the deformation, respectively. (b) The top 10% particles with high particle stress $\sigma_{zz}$. The particle color in (a) and (b) represents the number of particles of a cluster to which a particle belongs (see the color bar). (c) Mapping of the gyration radius $R_g$ as a function of the number of particles $N$ for clusters of the top 10% stressed (triangles) and strained (crosses) particles. The dotted and dashed lines have slopes of 3 and 1.5, respectively, representing the fractal dimensions of the top 10% stressed and strained particles. Panels (a)–(c) are results for external strain $\Delta\phi/\phi_0 = 0.0067$ from $\phi_0 = 0.3$. (d) The number of ruptured bonds $\Delta n_b^-$ under strain $\Delta\phi/\phi_0 = 0.0067$ for various $\phi_0$, normalized by the total number of bonds $n_b$. The red and blue curves are $\Delta n_b^-/n_b$ measured for the top 10% stressed and strained particles. The black curve represents the result for all bonds.

### E. Mechanical anisotropy of gels under uniaxial compression

Finally, we explore the structural and mechanical anisotropy of gels under uniaxial compression. The solid lines in Fig. 6(a) show the stress along the compression axis ($\sigma_{zz}$) and one perpendicular to it ($\sigma_{xx}$) for various volume fractions. The dotted lines in Fig. 6(a) represent the transient behaviors observed before the system enters a history-independent state from the initial conditions. We observe that for small $\phi$, the value of $\sigma_{zz}$ is significantly larger than that of $\sigma_{xx}$. However, the discrepancy between the two stresses diminishes as $\phi$ approaches $\phi_{\mathrm{RCP}}$. This suggests that the stress homogenization is induced by compression [71].

To investigate the structural features associated with the stress anisotropy, we first focus on the distribution of bond orientation $P(\hat{R}_z)$, where $\hat{R}_z$ is the amplitude of the $z$ component for the unit vector of each bond. Figure 6(b) shows $P(\hat{R}_z)$ for three different volume fractions ($\phi = 0.3$, 0.4, 0.5) in the history-independent state. Here, small ($\sim$0) and large ($\sim$1) values of $\hat{R}_z$ indicate that the bond direction is perpendicular and along the $z$ direction, respectively. The red and blue lines in Fig. 6(b) show $P(\hat{R}_z)$ for bonds that form and rupture within the strain $\Delta\phi/\phi_0 = 0.0069$, respectively. We observe that the bonds lying in the $xy$ plane and oriented to the $z$ axis tend to rupture, whereas those oriented along the $z$ axis tend to form. This behavior reflects the squeezing of the network along the $z$ direction by the external stress and the expansion in the $xy$ direction. Furthermore, we note that $P(\hat{R}_z)$ for all bonds (black) is almost flat, implying that the anisotropy of the static structure is weak.

This trend is also confirmed from the volume-fraction dependence of the characteristic pore size measured in $x$ and $z$ directions, $\ell_c^x$ and $\ell_c^z$; see Fig. 6(c). We find that $\ell_c^x$ and $\ell_c^z$ decrease similarly with increasing $\phi$, and the relative

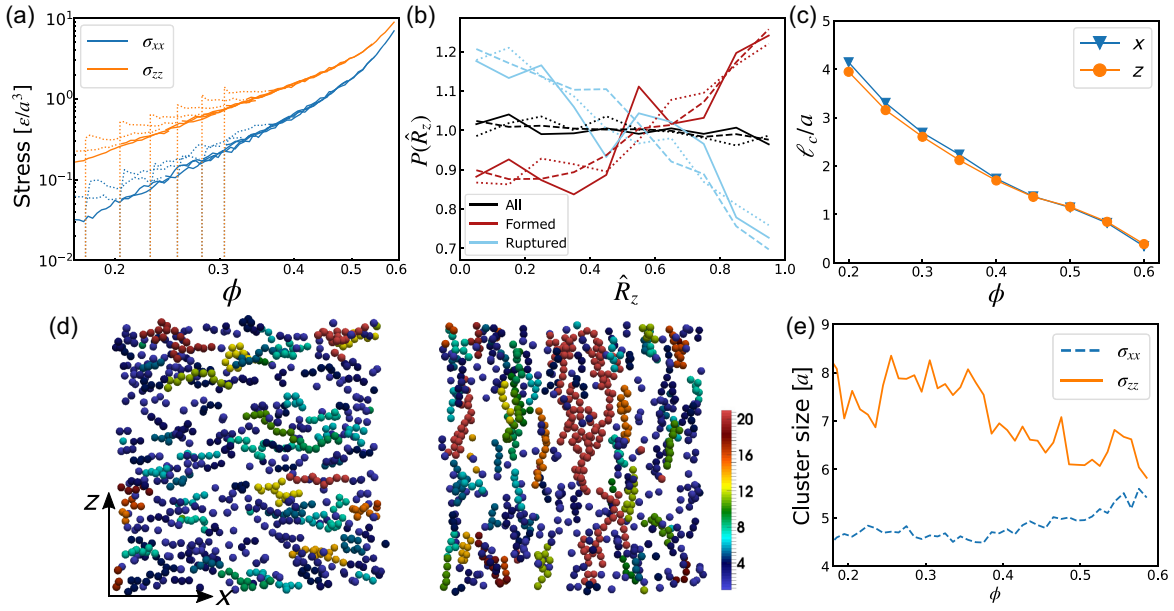


FIG. 6. Structural and mechanical anisotropy observed in uniaxial compression simulations. (a) The volume-fraction dependence of the stress $\sigma_{xx}$ (blue line) and $\sigma_{zz}$ (orange line) for various initial conditions ($\phi_{\mathrm{init}} = 0.175, 0.2, \ldots, 0.3$). The dotted and solid lines represent the results before and after absorbing into a history-independent state, respectively. (b) Distribution of the bond orientations $P(\hat{R}_z)$, where $\hat{R}_z$ is the magnitude of the $z$ component of the unit vector of a bond. The black lines represent $P(\hat{R}_z)$ for all bonds. The red and blue lines represent $P(\hat{R}_z)$ for bonds formed and ruptured within external strain $\Delta\phi/\phi_0 = 0.0069$. The solid, dotted, and dashed lines represent the results for $\phi_0 = 0.3$, 0.4, and 0.5, respectively. (c) Volume fraction dependence of the characteristic pore size for $x$ (triangle) and $z$ (circle) directions. (d) Snapshot of the top 10% stressed particles at $\phi = 0.4$ for $\sigma_{xx}$ (left) and $\sigma_{zz}$ (right). Particle color represents the number of particles of a cluster to which a particle belongs (see the color bar). (e) The volume-fraction dependence of the average cluster size for the top 10% stressed particles for $\sigma_{xx}$ (dashed line) and $\sigma_{zz}$ (solid line).

difference between them is at most ∼5%. This is consistent with the isotropic character of the microstructure observed in wet granular materials under gravity [23].

Then, we turn our attention to the mechanical structure discussed above. Figure 6(d) shows a snapshot of the top 10% stressed particles at $\phi = 0.4$ in terms of $\sigma_{xx}$ and $\sigma_{zz}$. We observe that chainlike clusters are present in both $xx$ and $zz$ components, but the clusters in the $xx$ component appear shorter than those in the $zz$ component. To quantify this observation, we calculate the average cluster size (see Appendix D for the definition) for $xx$ and $zz$ components at various $\phi$ values and present the results in Fig. 6(e). We find that the cluster size exhibits a significant difference between the two components for small $\phi$, and this difference decreases as $\phi$ approaches $\phi_{\mathrm{RCP}}$. These findings highlight the crucial role of the stress-bearing structure hidden in the nearly isotropic network structure in determining the mechanical anisotropy of the yield stress observed in Fig. 6(a).

## IV. CONCLUSION

In summary, we studied the microscopic structural features of particle networks during yielding under uniaxial compression. To elucidate the underlying microscopic mechanism, we employed confocal microscopy to observe the structural evolution of colloidal gels undergoing gravitational collapse, from individual particle trajectories to global sedimentation dynamics. We compared our experimental findings with the simulation results of the corresponding setting and those for very slow (almost quasistatic) uniaxial compression to establish the connection between the structural and mechanical properties of the particle networks.

We discovered that, despite substantial changes in the microstructure of the gel undergoing gravitational collapse with height and elapsed time, the gel's structure is statistically uniquely determined by the local volume fraction alone, independent of the deformation strain history that the system has experienced. However, the connection between structure and volume fraction is mildly affected by the preparation history of the initial conditions, including the volume fraction and age of the initial gel states. In contrast, the evolution of compressive stress follows a distinct function of the local volume fraction during compression, remaining unaffected by both the preparation and strain histories, except for the initial transient behavior, such as stress overshoot. Thus, the relation is robust as long as the interparticle interaction is identical.

This suggests a subtle retention of the memory of the initial structure during compressive yielding, while no such memory effect exists in the mechanical stress evolution. This retention of structural memory implies that the

compressive deformation erases only a part of memories encoded in the gel's initial microstructure by the control parameters, possibly reflecting the presence of both mechanically relevant and irrelevant local structural units. Nevertheless, the compressive stress remains uniquely determined by the local volume fraction, unaffected by such subtle differences in microstructures. These provide a clear indication of the mechanical self-organization of gels, independent of their preparation and strain history.

We uncovered the strain localization within isotropic clusters of network width and stress concentration on chainlike anisotropic clusters composed of stress-bearing particles. This process can be interpreted as the rearrangement of the network structure under mechanical constraints to support external stress, ultimately leading to mechanical self-organization into a history-independent absorbing state unique to compressive yielding.

These results offer novel microscopic insights into the nonlinear mechanical response of particulate network materials during compressive yielding, but they also raise many intriguing questions. For example, the elementary organizational processes of stress-bearing structures during compression are still unclear, and there has been limited exploration of the commonalities and differences between the microscopic processes involved in shear and compressive yielding [1–3].

It is important to note that the history-independent state observed in compressive yielding is not observed in shear yielding. In shear-induced yielding, the application of large shear strain or multiple cycles of oscillatory shear leads to failure in gels or slow coarsening of network strands, respectively (see, e.g., Refs. [7,10,11]). These observations highlight distinct behaviors and outcomes between shear and compressive yielding processes.

Furthermore, it is worth noting that this state is fundamentally different from the critical steady state observed in dense amorphous solids under unidirectional shear [12,60] and the absorbing state in non-Brownian suspensions [61,62] and granular materials [63,64] under cyclic shear. Unlike these cases, the state absorbed during compressive yielding continuously evolves with an increase in volume fraction, rather than remaining steady.

Notably, we found that $T1$ events play a minor role, and shear hand is absent during compressive yielding, indicating unique yielding behaviors of gels distinct from dense amorphous solids [12]. However, the volume fraction may increase significantly under strong compressive stress, leading to a homogeneous glassy state without voids [41,44]. Such a crossover of the yielding behavior from gels to attractive glasses, including their commonality and differences, is also an interesting topic for future study.

## ACKNOWLEDGMENTS

H. T. acknowledges the Grant-in-Aid for Specially Promoted Research (JSPS KAKENHI Grant No. JP20H05619) from the Japan Society for the Promotion of Science (JSPS). M. T. acknowledges the support from JSPS KAKENHI (Grants No. JP20K14424 and No. JP21KK0098). Y. W. acknowledges the support from Shanghai Jiao Tong University via the scholarship for outstanding Ph.D. graduates. The numerical calculations were partially performed on the Fujitsu PRIMERGY CX400M1/CX2550M5 (Oakbridge-CX) at the Information Technology Center, The University of Tokyo.

## APPENDIX A: SAMPLES

We synthesize poly(methyl methacrylate) (PMMA) colloids sterically stabilized with polyhydroxy steric acids and labeled with a fluorescent dye (Cy3) (see Ref. [47] for the detail). The diameter of the colloids is $a = 1.9$ μm with approximately 3% polydispersity. We use a mixture of *cis*-decahydronaphtalene (CIS) and cyclohexyl bromide (CHB) as a solvent. Because the refractive indexes of PMMA, CIS, and CHB are almost the same (1.491, 1.481, and 1.495, respectively), the Van der Waals interaction between colloids can be safely neglected, independent of the ratio of CIS and CHB. The mass density is matched between the solvent and colloids when the weight fraction of CIS in the whole solvent is $w_{cis} \sim 24\%$. We add a salt (tetra-butylammonium bromide) to the samples to screen the electrostatic repulsion between colloids. Polymers (polystyrene, molecular weight $8.4 \times 10^6$ Da) are mixed to induce the depletion attraction between colloids. The range of the attraction $\Delta = 2R_g/a$ ($R_g$ is the gyration radius of polymers) is approximately 0.13 [46]. The concentration of the polymer in the solvent $C_p$ is used to control the strength of the depth of the attractive potential $\epsilon$, and the temperature is kept to 26 °C. For the colloidal volume fraction in our interest ($\phi_{init} \sim 0.19 \pm 0.01$), we find that phase separation occurs when $C_p > C_p^* \sim 0.25$ g/L.

## APPENDIX B: EXPERIMENTAL PROTOCOL

We used a specially designed sample cell to observe gelation and gravitational collapse processes in a controlled manner (Fig. 7). First, we prepared a density-matched colloidal suspension at $\phi_{init} = 0.19 \pm 0.01$, including

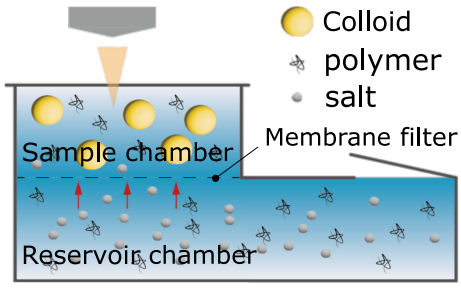


FIG. 7. Schematic of the sample cells used in our experiments. The cell is composed of sample and reservoir chambers, separated by a membrane filter.

polymers ($C_p = 0.5$ or 1.0 g/L) but without salt in the sample chamber. In this condition, the contacts between colloids are hardly observed due to the long-range Coulomb repulsion between colloids. Then, we inserted a solvent saturated with salt (density and polymer concentration being the same as those in a sample chamber) into the reservoir chamber to bring the two chambers into contact through a semipermeable membrane filter (Wahtman Anodisc 47, pore size 0.1 μm). This initiates the gentle but rapid injection of salt ions into the sample chamber through thermal diffusion, which screens the electric repulsion between colloids, allowing us to bring the sample from a stable one-phase state to an unstable two-phase state. The volume of the sample chamber is approximately $12\ \text{mm} \times 5\ \text{mm} \times 100a$, which is about $1/500$ times of one for the reservoir chamber. Once the salt injection screens the intercolloidal electrostatic interaction, colloids start to aggregate due to the polymer-induced depletion attraction, eventually (after about 1 h) forming an arrested gel (Fig. 1). The validity of this salt-injection method has been demonstrated in Refs. [45–47]. Then, we replaced the solvent in the reservoir chamber with a density-mismatched solvent ($w_{cis} = 16\%, 20\%, 32\%$) with salt and the same $C_p$ to apply the desired strength of the gravitational force on colloids ($\text{Pe} = 0.32, 0.16, -0.32$). We define the sign of Pe (or $\Delta\rho$) such that positive and negative values correspond to the floating and sedimentation of gels, respectively. This protocol allows us to observe gelation and collapse processes perfectly separately (Fig. 2).

## APPENDIX C: IMAGE ACQUISITION AND PARTICLE TRACKING

We employ a confocal laser scanning microscope (Leica SP5) to capture the positions of colloids in three-dimensional space. We use the scanned window with $56^3a^3$ for the gelation process and observe the middle part of the sample chamber. For the collapse process, we locate the scanned window with $56^2 \times 100a^3$ to cover the sample chamber from top to bottom along the $z$ axis (i.e., the gravitational axis). The thickness of the sample cell is maximized to accommodate the working distance of the lens used. The pixel size of the confocal image is $(0.21\ \mu\text{m})^3$, and the acquisition time for one frame is $\Delta t_{\text{scan}} = 24$ and 41 sec for the gelation and collapse observations, respectively. We note that this time duration is fast enough to track the sedimentating colloidal networks. We used the algorithm in Ref. [72] to detect the particle positions $\boldsymbol{R}_i(t)$ form a 3D confocal image. However, the particle displacement between two subsequent consecutive frames was not small enough to perform the particle identification by a simple comparison of the distance between $\boldsymbol{R}_i(t)$ and $\boldsymbol{R}_j(t + \Delta t_{\text{scan}})$. Then, we perform a kind of 3D particle image velocimetry combining $\boldsymbol{R}_i(t)$ and the original confocal image: to track particle $i$, we first extract a 3D cubic image with a side length 20 pixels centered on $\boldsymbol{R}_i(t)$ [Fig. 8(a)] from the original confocal image at time $t$. Next, using a template matching algorithm in OpenCV, we search for the most correlated 3D cubic image with the same size [see the images surrounded by the dashed squares in Fig. 8(b)] in the confocal image at time $t + \Delta t_{\text{scan}}$. We evaluate the distance from the center position of the detected 3D cubic image to the position of particle $j$, $\boldsymbol{R}_j(t + \Delta t_{\text{scan}})$. Then, we identify particle $j$, which is closest to the center of the detected cubic image (surrounded by the dashed squares) as particle $i$ at time $t + \Delta t_{\text{scan}}$ [see the circle in Fig. 8(c)].

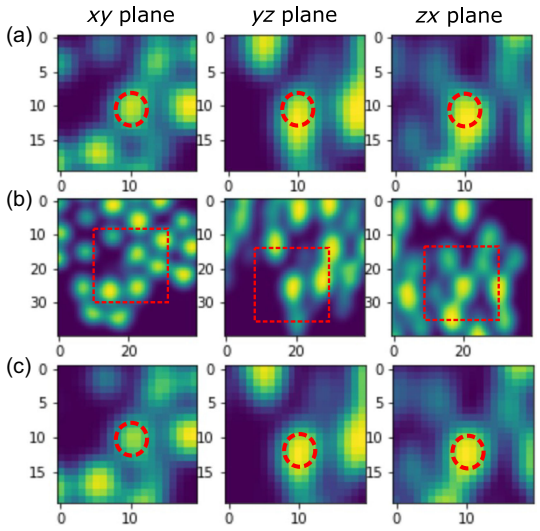


FIG. 8. Particle tracking using template matching. (a) The template 3D image for the tracking of particle $i$, $\boldsymbol{R}_i(t)$ (marked by dashed circles). Note that the center of each image is located at the center of the particle surrounded by the dashed circle. (b) The target of template matching (a part of the confocal image at time $t + \Delta t_{\text{scan}}$). The regions surrounded by the dashed squares mark the detected regions using template matching with the images in (a). (c) Enlargement of the detected 3D image. Dashed circles represent the position of particle $j$, $\boldsymbol{R}_j(t + \Delta t_{\text{scan}})$, which is closest to the center position of the detected cubic image surrounded by the dashed squares.

## APPENDIX D: ANALYSIS METHODS

### 1. Clustering analysis

We regard a pair of particles $(i, j)$ as bonded and belonging to the same cluster if the interparticle distance $R_{ij}$ is less than a threshold $R_{\text{th}}$. In simulations, the threshold is defined as the attraction range [$R_{\text{th}} = (1 + \Delta)a$]. On the other hand, in experiments, we set the threshold as $R_{\text{th}} = 1.2a$, due to experimental uncertainties such as the particle size polydispersity (∼3%), particle-tracking ambiguity, and optical diffraction; this threshold value approximately corresponds to the first minima of the radial distribution function. The average cluster size in Fig. 6(e) is defined by the second moment of the cluster size distribution divided by its first moment.

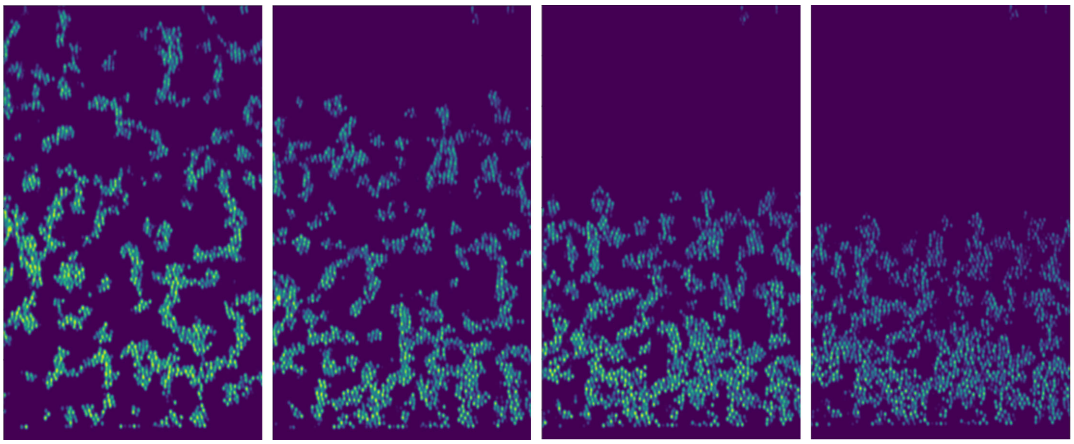

FIG. 9. A typical gravitational collapse process of a colloidal gel. The $xz$ section of the confocal image is shown for different times ($t = 0$, 23.1, 57.8, 115.6 min) at $C_p/C_p^* = 2$, Pe = 0.32.

### 2. Volume-fraction profile and chord length distribution

The volume-fraction profile along the compressive ($z$) axis, denoted as $\phi(z)$, is obtained by calculating the average value of $\phi(\mathbf{r})$ over the $xy$ plane. Here, $\phi(\mathbf{r})$ is a volume-fraction field constructed through a Gaussian kernel with a standard deviation of $\Delta_{cg} = a/2$. Specifically, $\phi(\mathbf{r}) = (\pi a^3/6)\rho_{cg}(\mathbf{r})$, where $\rho_{cg}(\mathbf{r}) = \sum_i \exp(-|\mathbf{r}-\mathbf{R}_i|^2/2\Delta cg^2)/(2\pi\Delta_{cg}^2)^{3/2}$.

To characterize the typical length at the network scale, we use the chord length distribution for the colloid-poor region $P(\ell)$. We define the region to satisfy $\rho_{cg} < \rho_{th}$ as the colloid-poor region. Here, $\rho_{th}$ is set as $e^{-1}(2\pi\Delta_{cg}^2)^{-3/2}$. We randomly choose a point on the colloid-poor region and draw a straight line from that point until the line hits the boundary of the colloid-rich and -poor regions. The line length corresponds to $\ell$ [see the inset of Fig. 1(d)]. The mean value of $P(\ell)$ corresponds to the characteristic pore size $\ell_c$.

### 3. Microscopic strain and stress

The microscopic shear strain of particle $i$ from the reference time $t_0$ during the interval $t_1$, denoted as $\gamma_i$, is defined by the difference between the maximum and minimum eigenvalues of the matrix $(e_i + e_i^T)/2$, where $e_{i,\alpha\beta} = X_{i,\alpha\gamma}Y_{i,\gamma\beta}^{-1} - \delta_{\alpha\beta}$ with $X_{i,\alpha\beta} = \sum_j [R_{j,\alpha}(t_0+t_1) - R_{i,\alpha}(t_0+t_1)][R_{j,\beta}(t_0) - R_{i,\beta}(t_0)]$ and $Y_{i,\alpha\beta} = \sum_j [R_{j,\alpha}(t_0) - R_{i,\alpha}(t_0)][R_{j,\beta}(t_0) - R_{i,\beta}(t_0)]$ [68]. The summation of the index $j$ is performed over the particles bonded with particle $i$ (here, the threshold $R_{th}$' is set to 1.3 both for experiments and simulations). The macroscopic stress $\sigma_{\alpha\beta}$ is computed using the virial stress formulation: $\sigma_{\alpha\beta} = -\sum_{i<j} R_{ij,\alpha}F_{ij,\beta}/V$, where $\boldsymbol{R}_{ij}$ and $\boldsymbol{F}_{ij}$ denote the relative position vector and interparticle force between particle $i$ and $j$, respectively. The microscopic stress for particle $i$ is defined as $\sigma_{i,\alpha\beta} = -\sum_j R_{ij,\alpha}F_{ij,\beta}$.

## APPENDIX E: INFLUENCE OF SOLVENT MOTION ON THE COLLAPSING PROCESS

To see the influence of solvent flow on the gravitational collapse processes, we use the fluid particle dynamics (FPD) method [73,74] and compare the numerical results to those obtained from Brownian dynamics methods. In short, this FPD method treats a solid colloidal particle as an undeformable fluid particle whose viscosity is much higher than the solvent viscosity. The viscosity $\eta$ changes smoothly across the colloid-solvent boundary as $\eta(\boldsymbol{r}) = \eta_c \sum_i \phi_i + \eta_s(1 - \sum_i \phi_i)$, through a particle field $\phi_i(\boldsymbol{r}) = s(|\boldsymbol{r} - \boldsymbol{R}_i|; r_{FPD}, \xi_{FPD})$, where we use $s(x; r_{FPD}, \xi_{FPD}) = \{\tanh[(r_{FPD} - x)/\xi_{FPD}] + 1\}/2$ ($r_{FPD}$ and $\xi_{FPD}$ being particle radius and interfacial thickness, respectively). This treatment allows us to follow the colloidal dynamics, including many-body hydrodynamic interactions (HIs), simply by solving the incompressible Navier-Stokes equation for fluid velocity $\boldsymbol{v}$ in a Cartesian coordinate system without suffering from the solid-fluid moving boundary condition. See Refs. [73,74] for details. We introduce a wall by locating a flat "viscous wall" with thickness $h_w$ perpendicular to the $z$ axis at $z = z_w$, described by a wall field $\phi_w(\boldsymbol{r}) = s(|z - z_w|; h_w/2, \xi_{FPD})$. Then, we solve the equations with the periodic boundary condition. To satisfy the boundary condition between wall and solvent, we enforce $\boldsymbol{v} = 0$ on the walls by adding a body force $\boldsymbol{f}_w(\boldsymbol{r}) = -\zeta_w\phi_w\boldsymbol{v}$, as implemented in the other types of the direct Navier-Stokes simulations; see, e.g., Ref. [75]. We performed FPD simulations on a Nvidia A40 GPU using the same units and parameter setting as in Refs. [46,74] under the athermal condition. We fixed $F_g = 12$, $\zeta_w = 200$, and $h_w = 6r_{FPD}$. The system size, interparticle potential, and initial condition are common to those in the Brownian dynamics simulations (the resulting computational grid size being $256 \times 256 \times 718$).

Figures 10(a) and 10(b) show the temporal change of the front height $h$ (i.e., the distance from the bottom wall to the

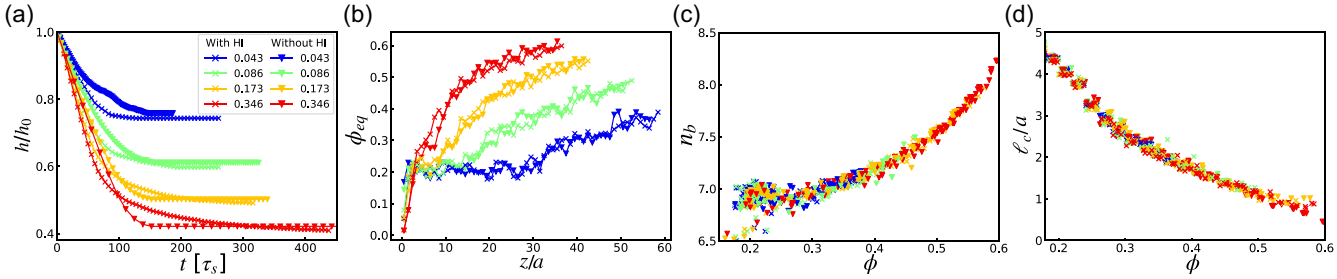


FIG. 10. Comparison between simulation results with and without hydrodynamic interactions (HIs). (a) Time evolution of height $h$, i.e., the distance from the bottom wall to the front of gel, for various $F_g$. $h$ is scaled by its initial value at $t = 0$, $h_0$. (b) Volume-fraction profiles in mechanical equilibrium states $\phi_{\rm eq}$ for various $F_g$. These results are obtained from athermal simulations for gels prepared at $T = 0.143$ and $\phi_{\rm init} = 0.2$. (c),(d) $\phi$ dependencies of the average coordination number per particle $n_b$ and the characteristic pore size $\ell_c$, respectively. The notation of symbols in (b)–(d) is the same as in (a).

front of a gel) and the mechanical equilibrium (or final) volume-fraction profile $\phi_{\rm eq}$, respectively, for various $F_g$. We use the Stokes time $\tau_s = \zeta a/2F_g$ as the time unit, where $\zeta$ is the friction coefficient of a free particle. $h$ is scaled by its initial value at $t = 0$, $h_0$. Here, we see that although $h$ evolves differently, depending on with and without HIs, $\phi_{\rm eq}$ is independent of it. This indicates that HIs significantly affect sedimentation speed but play a minor role in the microstructure. In other words, the solvent backflow is not strong enough to alter the microstructure in the current range of $F_g$ ($\lesssim 0.346$) and $h_0 = 100a$. In Figs. 10(c) and 10(d), mapping of $\phi$-$n_b$ and $\phi$-$\ell_c$ for various $(z, t)$ and $F_g$ is shown as in Fig. 3. Results obtained from simulations with and without HIs are almost identical, further supporting that HIs have little effect on microstructure.

## APPENDIX F: LOCAL CORRELATION BETWEEN VOLUME FRACTION AND STRESS IN UNIAXIAL COMPRESSION SIMULATIONS

Figure 11(a) illustrates the evolution of the volume-fraction profile $\phi(z)$ along the $z$ axis obtained from uniaxial compression simulations. Here, $z$ and $\phi(z)$ are scaled by the system size $L_z$ and the global (average) volume fraction $\phi^g$, respectively. The profile $\phi(z)$ is globally relatively uniform, and the amplitude of spatial fluctuations around the mean value ($\phi^g$) decreases as the compression proceeds. This can be interpreted simply as the parts of gels with smaller $\phi(z)$ being mechanically weaker and more likely to yield [i.e., increase $\phi(z)$], leading to density homogenization. This physical description is supported by the one-to-one correspondence and proportionality between $\phi(z)/\phi^g$ and $\sigma_{zz}(z)/\sigma^g_{zz}$, where $\sigma^g_{zz}$ is the global stress, as shown in Fig. 11(b). This local proportionality allows us to characterize the state of gels by the global volume fraction and conduct structural and mechanical analyses for the entire system in uniaxial compression simulations.

It is worth noting that the amplitude of spatial fluctuations in $\phi(z)$ and, consequently, in $\sigma_{zz}(z)$, is expected to diminish as the system size in the $xy$ plane expands. In the limit of infinite size, these fluctuations are anticipated to vanish entirely.

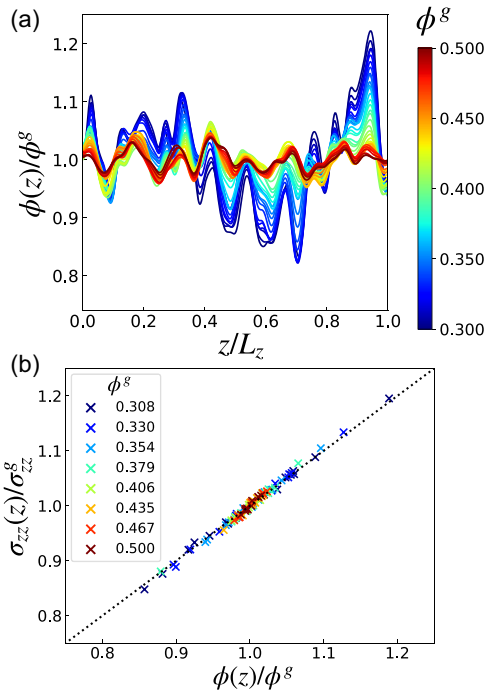


FIG. 11. Evolution of local volume fraction and stress in uniaxial compression simulations. (a) The evolution of volume-fraction profile $\phi(z)$ during uniaxial compression, scaled by the global volume fraction $\phi^g$. The results are obtained under athermal conditions for a gel prepared at $T = 0.143$ and $\phi_{\rm init} = 0.25$. We choose the range of $\phi^g$ to be 0.3–0.5, representing a history-independent state. (b) Scatter plot of $[\phi(z)/\phi^g, \sigma_{zz}(z)/\sigma^g_{zz}]$ measured at layers with a width of $3.5a$, where $\sigma^g_{zz}$ denotes the global stress. The dotted line represents a relation of $\sigma_{zz}(z)/\sigma^g_{zz} = \phi(z)/\phi^g$.

## APPENDIX G: EVOLUTION OF LOCAL STRUCTURES

Here, we analyze the evolution of several structural motifs identified by topological cluster classification (see, e.g., Refs. [65,66] for more details). The classification of microscopic structures is rooted in the concept of locally favored structures (LFSs), which denotes the smallest potential energy configuration among a limited set of possible arrangements. We specifically focus on the number densities of three local structures: tetrahedral ($n_3$), square pyramid ($n_4$), and pentagonal pyramid ($n_5$), which serve as building blocks to compose LFSs. From a mechanical viewpoint, the tetrahedral structure is stable, representing the LFS for four particles, as it minimizes the total interparticle potential. In contrast, the square pyramid is considered mechanically unstable because it can easily transition to an LFS consisting of two tetrahedra (the LFS for five particles) with minimal mechanical perturbation. The pentagonal pyramid is not a locally stable structure but can be regarded as mechanically relatively stable. This is because this local structure is similar to the LFS for seven particles (pentagonal bipyramid) and requires multiple sequential rearrangements to reach the LFS for six particles.

The experimental results, as depicted in Figs. 12(a)–12(c), faithfully reproduce the absorbing behavior observed in $n_b$ and $\ell_c$, as long as the initial conditions are common. This provides compelling evidence that the evolution of gel microstructures during uniaxial compression for the same $\phi_{\rm init}$ precisely follows the history-independent state.

On the other hand, Figure 12(d) presents the results obtained from uniaxial compression simulations for three distinct $\phi_{\rm init}$ values. Remarkably, $n_3$ and $n_5$ follow master curves nearly independent of $\phi_{\rm init}$. In contrast, this trend is not observed for $n_4$. These trends are consistent with the slight mismatch observed in the evolution of $n_b$ and $\ell_c$ among different $\phi_{\rm init}$ values, suggesting that, during compressive yielding, there is a selective involvement of mechanically relevant structures in the self-organization processes, rather than all types of local structures. However, at this moment, the direct link between these local structures and the mechanical structures (yielding compact and stress-bearing chain structures) discussed in Figs. 4 and 5 is unclear.

## APPENDIX H: AGING-TIME DEPENDENCE

As we discussed in Sec. III C, the influence of $\phi_{\rm init}$ on gel's microstructure is minor (but non-negligible), whereas it significantly depends on $\epsilon/k_{\rm B}T$. Here, we examine the aging-time ($t_{\rm age}$) dependence on the evolution of $n_b$, $\ell_c$, and $\sigma_{zz}$; the results are shown in Fig. 13. Similar to the case of $\phi_{\rm init}$, $t_{\rm age}$ alters the structural evolution slightly, but it does not affect the stress evolution. All the relevant simulation results presented in the main text were obtained at $t_{\rm age}/\tau_B = 3.0 \times 10^3$.

The longest aging time investigated in this section ($t_{\rm age}/\tau_B = 3.0 \times 10^5$) corresponds to a week in experimental terms. Maintaining the density matching condition over this extended period is challenging in our experimental setup, although it may be achievable through experiments conducted under microgravity conditions in space stations. It is important to note that physical colloidal gels are intrinsically in a nonequilibrium state, formed through arrested phase separation. Consequently, they eventually settle into a thermodynamically equilibrium state (gas-crystal coexistence) over a significantly longer timescale, which is beyond the scope of our study. For these reasons, we can reasonably conclude that the influence of aging time $t_{\rm age}$ is minor in the compressive yielding of colloidal gels.

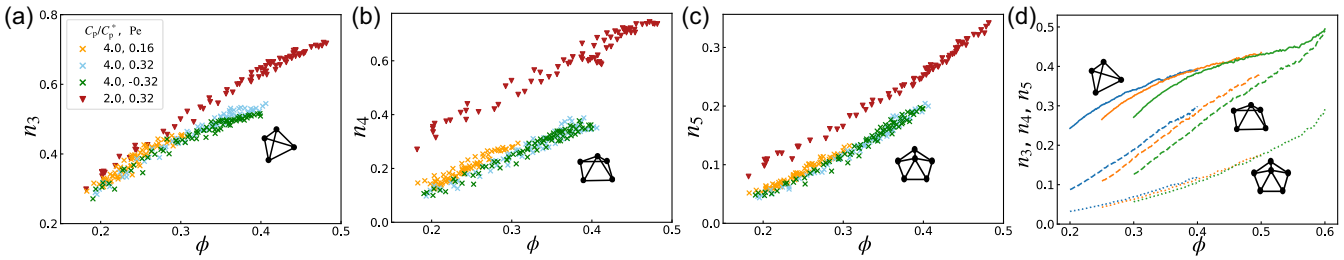


FIG. 12. Local structures of gels during compressive yielding. (a)–(c) Experimental results. $n_3$, $n_4$, and $n_5$ are the number densities (per volume) of the tetrahedral (three-ring), square pyramid (four-ring), and pentagonal pyramid (five-ring) structures. The brown cross, blue cross, green cross, and red triangle symbols represent the trajectory at $(C_{\rm p}/C_{\rm p}^*, {\rm Pe}) = (4, 0.16)$, $(4, 0.32)$, $(4, -0.32)$, and (2,0.16), respectively [the same trajectories used for Figs. 3(a)–3(c)]. (d) Results obtained from uniaxial compression simulations. Solid, dashed, and dotted lines indicate $n_3$, $n_4$, and $n_5$ for three different initial volume fractions $\phi_{\rm init} = 0.2$ (blue), 0.25 (orange), 0.3 (green) during uniaxial compression. Here, the simulation results for $T = 0.071$ [the same trajectories used for Figs. 3(d)–3(f)] are shown.

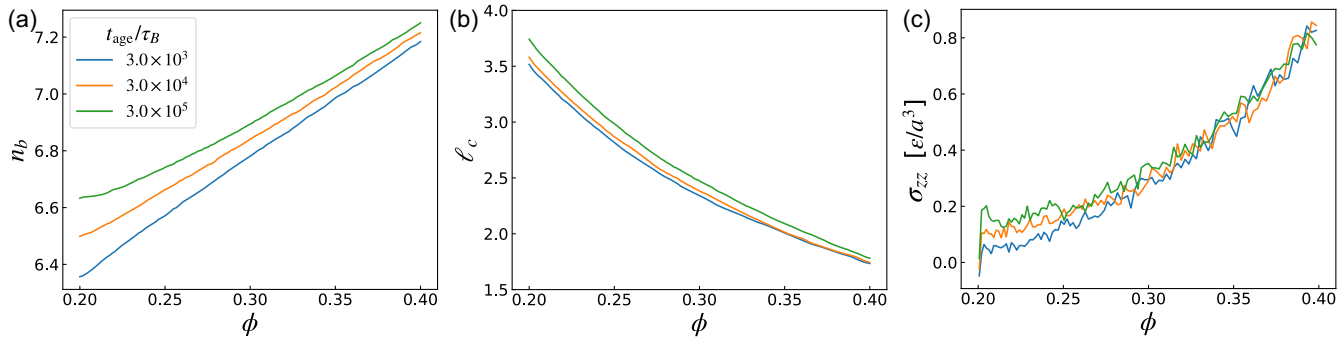


FIG. 13. The aging-time dependence of the structural and mechanical evolution during uniaxial compression. The evolution of (a) the average coordination number $n_b$, (b) the characteristic chord length $\ell_c$, and (c) the $zz$ component of the stress $\sigma_{zz}$ are shown as a function of volume fraction $\phi$. The color indicates the aging time (or the waiting time of gelation; $t_{age} = 3.0 \times 10^3$, $3.0 \times 10^4$, and $3.0 \times 10^5$). The temperature and initial volume fraction are $T = 0.071$ and $\phi_{init} = 0.2$, respectively. All the relevant simulation results shown in the main text correspond to those at $t_{age}/\tau_B = 3.0 \times 10^3$.

## APPENDIX I: SUPPLEMENTAL FIGURES

Figure 14 shows the volume-fraction profile $\phi(z,t)$ and $z$ component of average velocity of colloids $u_z(z,t)$ for trajectories $(C_p/C_p^*, \mathrm{Pe}) = (4, 0.16), (4, 0.32), (4, -0.32)$.

Figure 15 shows the chord length distribution obtained from uniaxial compression simulation.

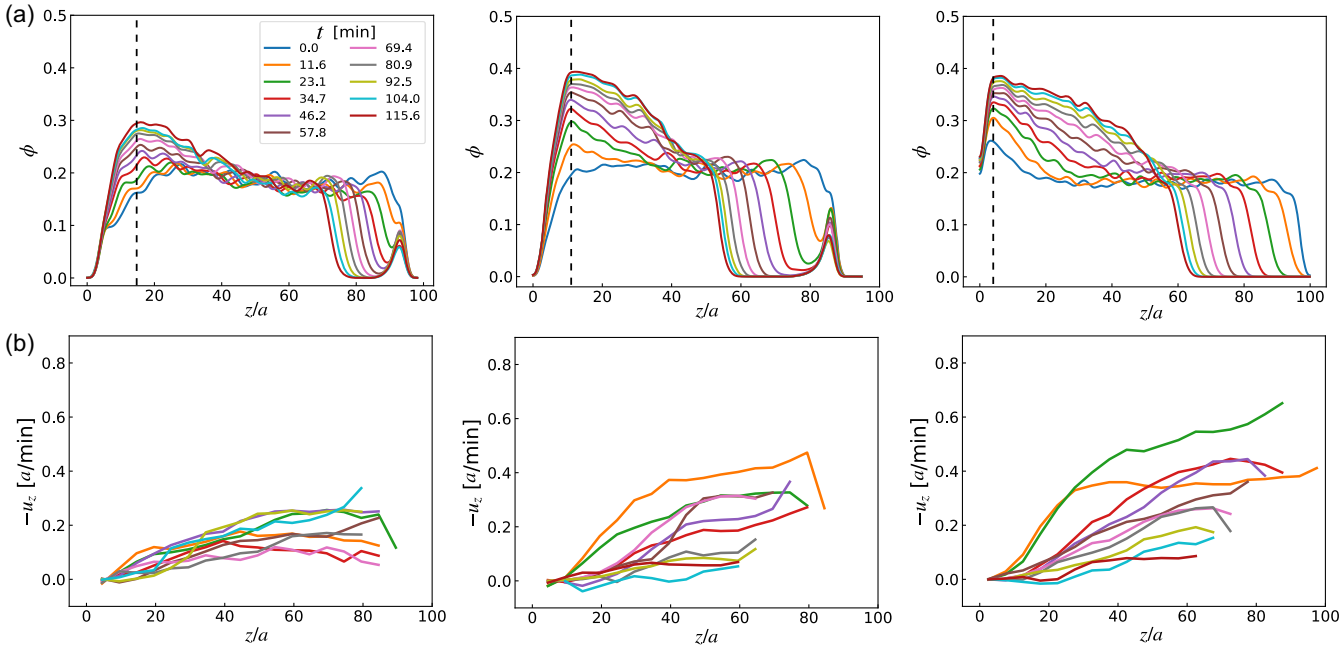


FIG. 14. Other examples of gravitational collapsing processes. (a) Volume-fraction profile $\phi(z,t)$ and (b) $z$ component of average velocity of colloids $u_z(z,t)$ for trajectories $(C_p/C_p^*, \mathrm{Pe}) = (4, 0.16), (4, 0.32), (4, -0.32)$ (left-hand, middle, and right-hand figures, respectively).

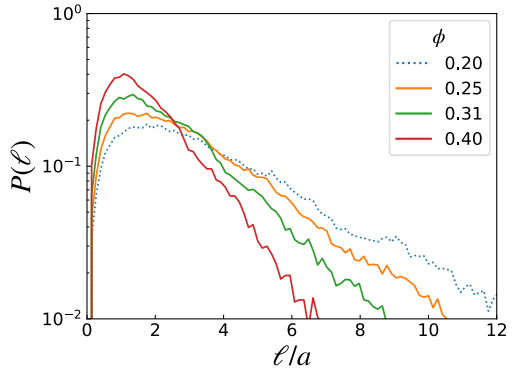


FIG. 15. Chord length distribution obtained from uniaxial compression simulation at $T = 0.143$ and $\phi_{\text{init}} = 0.2$. This parameter setting corresponds to the one for the experimental results shown in Fig. 3(c).

Figure 16 shows a comparison of $\sigma_{zz}(\phi)$ obtained from gravitational collapse (dots) and uniaxial compression (lines) simulations at zero temperature.

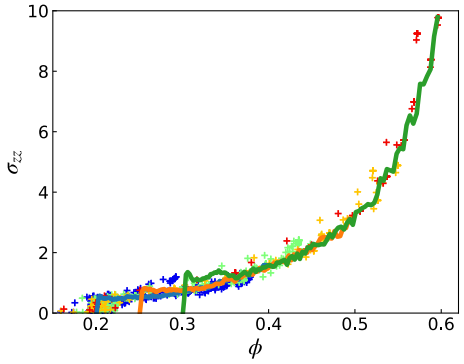


FIG. 16. The $\phi$ dependence of stress $\sigma_{zz}$ at zero temperature. Cross symbols represent the results of gravitational collapse simulations for gels prepared at $\phi_{\text{init}} = 0.2$ and $T = 0.143$. Each cross symbol corresponds to a map of $(\phi, \sigma_{zz})$ for a given pair of $(z, t)$. The color indicates the gravitational strength: $F_g = 0.043$ (blue), 0.086(green), 0.173 (brown), and 0.345 (red). Solid lines are the simulation results of uniaxial compression for three different initial conditions: $\phi_{\text{init}} = 0.2$ (blue), 0.25 (brown), and 0.3 (green).


[1] Emanuela Zaccarelli, *Colloidal gels: Equilibrium and non-equilibrium routes*, J. Phys. Condens. Matter **19**, 323101 (2007).

[2] C. Patrick Royall, Malcolm A. Faers, Sian L. Fussell, and James E. Hallett, *Real space analysis of colloidal gels: Triumphs, challenges and future directions*, J. Phys. Condens. Matter **33**, 453002 (2021).

[3] Daniel Bonn, Morton M. Denn, Ludovic Berthier, Thibaut Divoux, and Sébastien Manneville, *Yield stress materials in soft condensed matter*, Rev. Mod. Phys. **89**, 035005 (2017).

[4] P. A. Smith, G. Petekidis, S. U. Egelhaaf, and W. C. K. Poon, *Yielding and crystallization of colloidal gels under oscillatory shear*, Phys. Rev. E **76**, 041402 (2007).

[5] Esmaeel Moghimi, Alan R. Jacob, Nick Koumakis, and George Petekidis, *Colloidal gels tuned by oscillatory shear*, Soft Matter **13**, 2371 (2017).

[6] Poornima Padmanabhan and Roseanna Zia, *Gravitational collapse of colloidal gels: Non-equilibrium phase separation driven by osmotic pressure*, Soft Matter **14**, 3265 (2018).

[7] Andrew Clarke, *Gel breakdown in a formulated product via accumulated strain*, Soft Matter **17**, 7893 (2021).

[8] Lilian C. Hsiao, Richmond S. Newman, Sharon C. Glotzer, and Michael J. Solomon, *Role of isostaticity and load-bearing microstructure in the elasticity of yielded colloidal gels*, Proc. Natl. Acad. Sci. U.S.A. **109**, 16029 (2012).

[9] Nick Koumakis, Esmaeel Moghimi, Rut Besseling, Wilson C. K. Poon, John F. Brady, and George Petekidis, *Tuning colloidal gels by shear*, Soft Matter **11**, 4640 (2015).

[10] Mohammad Nabizadeh and Safa Jamali, *Life and death of colloidal bonds control the rate-dependent rheology of gels*, Nat. Commun. **12**, 4274 (2021).

[11] Deepak Mangal, Mohammad Nabizadeh, and Safa Jamali, *Topological origins of yielding in short-ranged weakly attractive colloidal gels*, J. Chem. Phys. **158**, 014903 (2023).

[12] Alexandre Nicolas, Ezequiel E. Ferrero, Kirsten Martens, and Jean-Louis Barrat, *Deformation and flow of amorphous solids: Insights from elastoplastic models*, Rev. Mod. Phys. **90**, 045006 (2018).

[13] Albert Mihranyan, Natalia Ferraz, and Maria Strømme, *Current status and future prospects of nanotechnology in cosmetics*, Prog. Mater. Sci. **57**, 875 (2012).

[14] Thomas Gibaud, Damien Frelat, and Sébastien Manneville, *Heterogeneous yielding dynamics in a colloidal gel*, Soft Matter **6**, 3482 (2010).

[15] Teresa Liberto, Marie Le Merrer, Catherine Barentin, Maurizio Bellotto, and Jean Colombani, *Elasticity and yielding of a calcite paste: Scaling laws in a dense colloidal suspension*, Soft Matter **13**, 2014 (2017).

[16] Raffaele Mezzenga, Peter Schurtenberger, Adam Burbidge, and Martin Michel, *Understanding foods as soft materials*, Nat. Mater. **4**, 729 (2005).

[17] Jin Hyun Nam and Dong Hyup Jeon, *A comprehensive micro-scale model for transport and reaction in intermediate temperature solid oxide fuel cells*, Electrochim. Acta **51**, 3446 (2006).

[18] Mohamed Youssry, Lénaïc Madec, Patrick Soudan, Manuella Cerbelaud, Dominique Guyomard, and Bernard Lestriez, *Non-aqueous carbon black suspensions for lithium-based redox flow batteries: Rheology and simultaneous rheo-electrical behavior*, Phys. Chem. Chem. Phys. **15**, 14476 (2013).

[19] Xiaohu Xia, Zhibing Hu, and Manuel Marquez, *Physically bonded nanoparticle networks: A novel drug delivery system*, J. Control Release **103**, 21 (2005).

[20] Alexis Darras, Anil Kumar Dasanna, Thomas John, Gerhard Gompper, Lars Kaestner, Dmitry A Fedosov, and Christian

Wagner, *Erythrocyte sedimentation: Collapse of a high-volume-fraction soft-particle gel*, Phys. Rev. Lett. **128**, 088101 (2022).
[21] W. B. Dade, A. R. M. Nowell, and P. A. Jumars, *Predicting erosion resistance of muds*, Mar. Geol. **105**, 285 (1992).
[22] Douglas J. Jerolmack and Karen E. Daniels, *Viewing Earth's surface as a soft-matter landscape*, Nat. Rev. Phys. **1**, 716 (2019).
[23] Jindong Li, Yixin Cao, Chengjie Xia, Binquan Kou, Xianghui Xiao, Kamel Fezzaa, and Yujie Wang, *Similarity of wet granular packing to gels*, Nat. Commun. **5**, 5014 (2014).
[24] Emanuela Zaccarelli, Peter J. Lu, Fabio Ciulla, David A. Weitz, and Francesco Sciortino, *Gelation as arrested phase separation in short-ranged attractive colloid–polymer mixtures*, J. Phys. Condens. Matter **20**, 494242 (2008).
[25] W. C. K. Poon, Laura Starrs, S. P. Meeker, A. Moussaid, R. M. L. Evans, P. N. Pusey, and M. M. Robins, *Delayed sedimentation of transient gels in colloid–polymer mixtures: Dark-field observation, rheology and dynamic light scattering studies*, Faraday Discuss. **112**, 143 (1999).
[26] Laura Starrs, W. C. K. Poon, D. J. Hibberd, and M. M. Robins, *Collapse of transient gels in colloid-polymer mixtures*, J. Phys. Condens. Matter **14**, 2485 (2002).
[27] V. Gopalakrishnan, Kenneth S. Schweizer, and C. F. Zukoski, *Linking single particle rearrangements to delayed collapse times in transient depletion gels*, J. Phys. Condens. Matter **18**, 11531 (2006).
[28] Ji Yeon Huh, Matthew L. Lynch, and Eric M. Furst, *Microscopic structure and collapse of depletion-induced gels in vesicle-polymer mixtures*, Phys. Rev. E **76**, 051409 (2007).
[29] Richard Buscall, Tahsin H. Choudhury, Malcolm A. Faers, James W. Goodwin, Paul A. Luckham, and Susan J. Partridge, *Towards rationalising collapse times for the delayed sedimentation of weakly-aggregated colloidal gels*, Soft Matter **5**, 1345 (2009).
[30] Lisa J. Teece, Malcolm A. Faers, and Paul Bartlett, *Ageing and collapse in gels with long-range attractions*, Soft Matter **7**, 1341 (2011).
[31] Giovanni Brambilla, Stefano Buzzaccaro, Roberto Piazza, Ludovic Berthier, and Luca Cipelletti, *Highly nonlinear dynamics in a slowly sedimenting colloidal gel*, Phys. Rev. Lett. **106**, 118302 (2011).
[32] Paul Bartlett, Lisa J. Teece, and Malcolm A. Faers, *Sudden collapse of a colloidal gel*, Phys. Rev. E **85**, 021404 (2012).
[33] Lisa J. Teece, James M. Hart, Kerry Yen Ni Hsu, Stephen Gilligan, Malcolm A. Faers, and Paul Bartlett, *Gels under stress: The origins of delayed collapse*, Colloids Surf. A **458**, 126 (2014).
[34] Eleonora Secchi, Stefano Buzzaccaro, and Roberto Piazza, *Time-evolution scenarios for short-range depletion gels subjected to the gravitational stress*, Soft Matter **10**, 5296 (2014).
[35] Roberto Piazza, *Settled and unsettled issues in particle settling*, Rep. Prog. Phys. **77**, 056602 (2014).
[36] Rim Harich, T. W. Blythe, Michiel Hermes, Emanuela Zaccarelli, A. J. Sederman, Lynn F. Gladden, and Wilson C. K. Poon, *Gravitational collapse of depletion-induced colloidal gels*, Soft Matter **12**, 4300 (2016).
[37] Azaima Razali, Christopher J. Fullerton, Francesco Turci, James E. Hallett, Robert L. Jack, and C. Patrick Royall, *Effects of vertical confinement on gelation and sedimentation of colloids*, Soft Matter **13**, 3230 (2017).
[38] Richard Buscall, *The sedimentation of concentrated colloidal suspensions*, Colloid Surf. **43**, 33 (1990).
[39] J. J. Liétor-Santos, C. Kim, P. J. Lu, A. Fernández-Nieves, and D. A. Weitz, *Gravitational compression of colloidal gels*, Eur. Phys. J. E **28**, 159 (2009).
[40] Jize Sui, *Dynamic behaviors of sedimenting colloidal gel materials: Hydrodynamic interactions*, Phys. Chem. Chem. Phys. **22**, 14340 (2020).
[41] Chanjoong Kim, Yaqian Liu, Angelika Kühnle, Stephan Hess, Sonja Viereck, Thomas Danner, L. Mahadevan, and David A. Weitz, *Gravitational stability of suspensions of attractive colloidal particles*, Phys. Rev. Lett. **99**, 028303 (2007).
[42] Stefano Buzzaccaro, Roberto Rusconi, and Roberto Piazza, *"Sticky" hard spheres: Equation of state, phase diagram, and metastable gels*, Phys. Rev. Lett. **99**, 098301 (2007).
[43] Stefano Buzzaccaro, Eleonora Secchi, Giovanni Brambilla, Roberto Piazza, and Luca Cipelletti, *Equilibrium concentration profiles and sedimentation kinetics of colloidal gels under gravitational stress*, J. Phys. Condens. Matter **24**, 284103 (2012).
[44] Enrico Lattuada, Stefano Buzzaccaro, and Roberto Piazza, *Compressive yield stress of depletion gels from stationary centrifugation profiles*, J. Phys. Condens. Matter **30**, 044005 (2018).
[45] Hideyo Tsurusawa, Mathieu Leocmach, John Russo, and Hajime Tanaka, *Direct link between mechanical stability in gels and percolation of isostatic particles*, Sci. Adv. **5**, eaav6090 (2019).
[46] Michio Tateno and Hajime Tanaka, *Numerical prediction of colloidal phase separation by direct computation of Navier–Stokes equation*, npj Comput. Mater. **5**, 40 (2019).
[47] Michio Tateno, Taiki Yanagishima, and Hajime Tanaka, *Microscopic structural origin behind slowing down of colloidal phase separation approaching gelation*, J. Chem. Phys. **156**, 084904 (2022).
[48] Kathryn A. Whitaker, Zsigmond Varga, Lilian C Hsiao, Michael J. Solomon, James W. Swan, and Eric M. Furst, *Colloidal gel elasticity arises from the packing of locally glassy clusters*, Nat. Commun. **10**, 2237 (2019).
[49] S. Zhang, L. Zhang, M. Bouzid, D. Z. Rocklin, E. Del Gado, and X. Mao, *Correlated rigidity percolation and colloidal gels*, Phys. Rev. Lett. **123**, 058001 (2019).
[50] Joost De Graaf, Wilson C. K. Poon, Magnus J. Haughey, and Michiel Hermes, *Hydrodynamics strongly affect the dynamics of colloidal gelation but not gel structure*, Soft Matter **15**, 10 (2019).
[51] J. M. Kim, J. Fang, A. P. R. Eberle, R. Castaneda-Priego, and N. J. Wagner, *Gel transition in adhesive hard-sphere colloidal dispersions: The role of gravitational effects*, Phys. Rev. Lett. **110**, 208302 (2013).
[52] Richard Buscall and Lee R. White, *The consolidation of concentrated suspensions. Part 1. The theory of sedimentation*, J. Chem. Soc. Faraday Trans. **83**, 873 (1987).
[53] Matthew D. Green, Maria Eberl, and Kerry A. Landman, *Compressive yield stress of flocculated suspensions: Determination via experiment*, AIChE J. **42**, 2308 (1996).

[54] Matthew D. Green and David V. Boger, *Yielding of suspensions in compression*, Ind. Eng. Chem. Res. **36**, 4984 (1997).

[55] S. Manley, J. M. Skotheim, L, Mahadevan, and D. A. Weitz, *Gravitational collapse of colloidal gels*, Phys. Rev. Lett. **94**, 218302 (2005).

[56] Jean-Michel Condre, Christian Ligoure, and Luca Cipelletti, *The role of solid friction in the sedimentation of strongly attractive colloidal gels*, J. Stat. Mech. (2007) P02010.

[57] Ryohei Seto, Robert Botet, Martine Meireles, Günter K. Auernhammer, and Bernard Cabane, *Compressive consolidation of strongly aggregated particle gels*, J. Rheol. **57**, 1347 (2013).

[58] Saikat Roy and Mahesh S. Tirumkudulu, *Universality in consolidation of colloidal gels*, Soft Matter **12**, 9402 (2016).

[59] See Supplemental Material at http://link.aps.org/supplemental/10.1103/PhysRevX.14.011035 for the experimentally captured entire collapse process (Movie 1), experimental results illustrating the evolution of highly strained particles (Movie 2), simulation results depicting the evolution of highly strained/stressed particles (Movie 3), and simulation results regarding bond formation and rupture dynamics (Movie 4).

[60] Bruno Andreotti, Yoël Forterre, and Olivier Pouliquen, *Granular Media: Between Fluid and Solid* (Cambridge University Press, Cambridge, England, 2013).

[61] Ido Regev, Turab Lookman, and Charles Reichhardt, *Onset of irreversibility and chaos in amorphous solids under periodic shear*, Phys. Rev. E **88**, 062401 (2013).

[62] Ido Regev, John Weber, Charles Reichhardt, Karin A. Dahmen, and Turab Lookman, *Reversibility and criticality in amorphous solids*, Nat. Commun. **6**, 8805 (2015).

[63] David J. Pine, Jerry P. Gollub, John F. Brady, and Alexander M. Leshansky, *Chaos and threshold for irreversibility in sheared suspensions*, Nature (London) **438**, 997 (2005).

[64] Laurent Corte, Paul M. Chaikin, Jerry P. Gollub, and David J. Pine, *Random organization in periodically driven systems*, Nat. Phys. **4**, 420 (2008).

[65] C. Patrick Royall, Stephen R. Williams, Takehiro Ohtsuka, and Hajime Tanaka, *Direct observation of a local structural mechanism for dynamic arrest*, Nat. Mater. **7**, 556 (2008).

[66] Alex Malins, Stephen R. Williams, Jens Eggers, and C. Patrick Royall, *Identification of structure in condensed matter with the topological cluster classification*, J. Chem. Phys. **139**, 234506 (2013).

[67] Jun Dong, Francesco Turci, Robert L. Jack, Malcolm A. Faers, and C. Patrick Royall, *Direct imaging of contacts and forces in colloidal gels*, J. Chem. Phys. **156**, 214907 (2022).

[68] Michael L. Falk and James S. Langer, *Dynamics of viscoplastic deformation in amorphous solids*, Phys. Rev. E **57**, 7192 (1998).

[69] Yinqiao Wang, Yujie Wang, and Jie Zhang, *Connecting shear localization with the long-range correlated polarized stress fields in granular materials*, Nat. Commun. **11**, 4349 (2020).

[70] Yixin Cao, Jindong Li, Binquan Kou, Chengjie Xia, Zhifeng Li, Rongchang Chen, Honglan Xie, Tiqiao Xiao, Walter Kob, Liang Hong *et al.*, *Structural and topological nature of plasticity in sheared granular materials*, Nat. Commun. **9**, 2911 (2018).

[71] Yinqiao Wang, Jin Shang, Yujie Wang, Jie Zhang, *Contact force measurements and local anisotropy in ellipses and disks*, Phys. Rev. Res. **3**, 043053 (2021).

[72] John C. Crocker and David G. Grier, *Methods of digital video microscopy for colloidal studies*, J. Colloid Interface Sci. **179**, 298 (1996).

[73] Hajime Tanaka and Takeaki Araki, *Simulation method of colloidal suspensions with hydrodynamic interactions: Fluid particle dynamics*, Phys. Rev. Lett. **85**, 1338 (2000).

[74] A. Furukawa, M. Tateno, and H. Tanaka, *Physical foundation of the fluid particle dynamics method for colloid dynamics simulation*, Soft Matter **14**, 3738 (2018).

[75] Yasuya Nakayama and Ryoichi Yamamoto, *Simulation method to resolve hydrodynamic interactions in colloidal dispersions*, Phys. Rev. E **71**, 036707 (2005).